In: Cyclones: Formation, Triggers and Control ISBN
Editor: Kazuyoshi Oouchi and Hironori Fudeyasu, pp.

Chapter #

SYNOPTIC AND CLIMATIC ASPECTS OF TROPICAL CYCLOGENESIS IN WESTERN NORTH PACIFIC

Tim Li*

International Pacific Research Center and Department of Meteorology, University of Hawaii at Manoa, Honolulu, Hawaii, USA

Abstract

In this chapter I first describe various precursor synoptic signals prior to tropical cyclone genesis in the western North Pacific. Then I discuss the origin of the summertime synoptic-scale wave train in the western Pacific and the energy source and dispersion characteristics of Pacific easterly waves. Next I present two cyclogenesis modeling results, focusing on the energy dispersion of a preexisting tropical cyclone and genesis efficiency of mid-level versus bottom vortex. The climatologic aspect of the tropical cyclogenesis is discussed, with a focus on the large-scale control of the atmospheric intraseasonal oscillation (ISO) and El Nino-Southern Oscillation (ENSO). A methodology is developed to rank key cyclogenesis parameters at different basins. Finally I describe the robust signals of future TC projection in the North Pacific from high-resolution global model simulations.

1. Introduction

Tropical cyclone (TC) genesis is a process through which random cumulus-scale cloud systems are well organized under favorable large-scale conditions and develop into a warm-core, cyclonic system with sustainable winds. Due to the lack of reliable data over open oceans and complicated scale interactions involved, understanding of TC genesis remains very limited.

The western North Pacific (WNP) is the most frequent TC genesis region in the globe. The summer mean circulation in the WNP has some unique features. For example, the WNP is the region of the greatest warm pool in boreal summer, with averaged sea surface temperature (SST) being greater than 29^{o}C. The low-level circulation is characterized by a confluence zone between the monsoon westerly and the trade easterly. A meridional shear line along 150^{o}E, 5^{o}N and 120^{o}E, 20^{o}N

* E-mail address: timli@hawaii.edu

separates the westerly to the south and the easterly to the north. The maximum low-level convergence and cyclonic vorticity overlap with intense convection, forming the WNP monsoon trough. Such a mean flow feature differs distinctively from that in the North Atlantic (NATL).

While the summer mean circulation provides favorable environmental conditions for cyclogenesis, it is synoptic-scale disturbances that trigger individual cyclogenesis events. Recent advances in satellite observations make it possible to reveal detailed synoptic-scale circulation patterns associated with tropical cyclogenesis. In section 2, synoptic-scale precursor disturbances prior to the formation of TC in the WNP will be described based on the analysis of satellite and NCEP-NCAR reanalysis data. Different from the NATL where the major perturbation source is Africa easterly waves, precursor perturbations in the WNP include TC energy dispersion (TCED) induced Rossby wave trains, northwest-southeast oriented synoptic wave trains (SWT), and Pacific easterly waves (PEW).

The origins of the synoptic wave trains and Pacific easterly waves are discussed in section 3. This is followed by the numerical modeling of cyclogenesis in section 4. First the process through which TCED induced Rossby wave train interacting with a monsoon gyre leads to the formation of a new TC is discussed. Next, given an environmental mid-level or bottom vortex initially, how the TC-scale vortex is developed and organized from random cumulus-scale clouds is further diagnosed with cloud-resolving model simulations. The genesis efficiency under the environmental mid-level and bottom vortex is compared.

From a climatologic aspect, what determines the TC genesis frequency in WNP? Can the same set of parameters determine the cyclogenesis in both the WNP and NATL? In section 5 the large-scale control of TC genesis by the atmospheric ISO and ENSO is discussed first. A methodology is then introduced to quantitatively measure the relative importance of genesis parameters in the NATL and WNP.

How Pacific TC frequency changes under global warming is addressed in section 6 through the diagnosis of two high-resolution global atmospheric general circulations models (AGCMs), forced with different future SST warming patterns. Both the models project a marked west-east shift in the North Pacific, with a large decrease (increase) of TC genesis number in the western (central) Pacific. The mechanism responsible for the distinctive regional TC changes is further discussed.

2. Precusor synoptic signals prior to cyclogenesis

The structure and evolution characteristics of tropical perturbations prior to TC formation in the WNP during 2000-2001 summers were investigated through the analysis of QuikSCAT, TMI and other observational data. Thirty-four TC genesis events were identified in the boreal summers of 2000 and 2001. Among 34 TCs, six (20%) are associated with TCED, eleven cases (30%) are associated with SWT (including those originated from equatorial mixed Rossby-gravity waves), and seven cases (20%) are associated with PEW. In the following I describe these and additional genesis scenarios.

a. Cyclogenesis in the wake of a preexisting TC due to TCED

The first type synoptic-scale disturbance associated with TC genesis in the WNP is Rossby wave energy dispersion from a preexisting TC (TCED). A vortex is subject to Rossby wave energy dispersion even in a simple barotropic framework. While a vortex moves northwestward due to the mean flow steering and the planetary vorticity gradient, Rossby waves emit energy southeastward [1-5]. As a result, a Rossby wave train with alternating anticyclonic and cyclonic vorticity perturbations forms in its wake [6-7]. A study of three-dimensional (3D) Rossby wave energy dispersion showed that TCED-induced Rossby wave train has a baroclinic structure and that the upper-level wave train develops rapidly and triggers downward energy propagation that enhances the lower level Rossby wave train [8].

Cyclogenesis due to TCED was suggested previously [9-12] without a detailed description of the wave train structure and evolution. Using the satellite data, Li et al. showed the Rossby wave train pattern and its connection with cyclogenesis [13]. Among the 34 cases identified in the summers of 2000-2001, six cyclogenesis cases are associated with TCED. Figure 1 illustrates an example. It shows the evolution of the 3-8 day filtered QuikSCAT wind fields from 1 August to 9 August 2000. Letter “A” in Fig. 1 represents the location of Typhoon Jelawat that formed on August 1. During the first 2-3 days, due to its weak intensity, Jelawat did not generate a visible Rossby wave train in its wake. During its northwestward journey, the intensity of Jelawat increased. With its steady intensification, the Rossby wave train became more and more evident in its wake. On 6 August, a clear wave train was observed. This Rossby wave train has a zonal wavelength of about 2500 km, oriented in a northwest-southeast direction.

The most remarkable characteristic of this wave train is that it had a large meridional wavelength. A half meridional wavelength was about 4000 km on 6 August. The meridional wavelength of the wave train was greatly reduced in subsequent days, leading to generation of a new TC on 9 August. Note that this

new TC Ewiniar (represented by letter "B" in Fig. 1) formed in the cyclonic vorticity center of the Rossby wave train.

The vertical profile of the Rossby wave train produced by TCED was examined with 3-8-day filtered NCEP-NCAR reanalysis data at different levels [14]. There was no clear wave pattern at 200hPa, but the wave train was evident at middle and lower troposphere with little vertical tilt. The cyclonic circulation region of the wave train coincided well with the region of concentrated cloud liquid water, whereas the anticyclonic circulation region of the wave train was cloud-free.

It was noted that some TCs did not reproduce a Rossby wave train in their wakes. Whether or not a TC generates a Rossby wave train depends on TC size or intensity [15-16], its radial wind profile [17], and its environmental flow such as vertical shear [18]. Whether or not a new TC can form in the Rossby wave train depends on the background flow the wave train is embedded in. A larger environmental low-level cyclonic vorticity and/or a larger environmental low-level convergence may favor cyclogenesis in the Rossby wave train [16, 19].

b. TC genesis associated with SWT

The second type of TC genesis happens within a synoptic wave train (SWT) that does not involve a preexisting TC. An observational study by Lau and Lau showed that the dominant synoptic-scale mode in the summertime WNP is a northwest-southeast oriented wave train, which has a typical wavelength of ~2500 km and propagates northwestward [20]. The intensity of the SWT increases as they move northwestward from the lower latitudes to the WNP.

During 2000 and 2001 summers, there were eleven TCs that formed in the SWT. An example is illustrated here for the formation of Typhoon Manyi, formed on 2 August 2001 (Fig. 2). Three days prior to its genesis, a northwest-southeast oriented wave train developed in the WNP. This wave train had well-defined cyclonic and anticyclonic circulations, and covered a region between 130^{o}E-160^{o}E and 0^{o}N-25^{o}N. The wave train moved slowly northwestward. On 2 August, Manyi developed in the cyclonic vorticity region of the wave train.

Among the eleven SWT-induced cyclogenesis cases, four were associated with equatorial MRG waves. The MRG wave has an equatorially anti-symmetric structure with pronounced clockwise cross-equatorial flow. An example is given for Typhoon Sepat (see Fig. 7 of [14]). An equatorial MRG wave appeared on 24 August 2001 near the date line. As its phase propagates westward, the group velocity of the MRG wave was eastward. This led to the development of the second MRG wave to its east, which had counter-clockwise flow. Meanwhile, the original MRG wave deviated to the north of the equator. This led to the development of a northwest-southeast oriented wave train in the WNP. The wave

train was clearly seen in the 3-8-day filtered wind field on 26 August. As the wave train continued to develop, a new TC named Sepat formed in the cyclonic vorticity region of the wave train on 27 August. Such a transition process from an equatorial MRG wave to off-equator tropical depression (TD)-type disturbances is consistent with previous studies [21-22].

c. TC genesis associated with easterly waves

The third type of cyclogenesis in the WNP is associated with the development of Pacific easterly waves (PEW). Different form African easterly waves, the energy source of the PEW comes from mid-latitude Jet (a specific discussion of this subject will be given in section 3). During 2000-2001 summers, seven PEW-induced cyclogenesis cases were identified. Only cyclogenesis cases that were associated with clear westward propagation signals in both the perturbation kinetic energy and rainfall fields derived from the TMI data were considered as PEW-induced cyclogenesis cases.

An example of PEW induced TC genesis is given for Typhoon Kong-rey, which formed on 22 July 2001. Figure 3 shows the time-longitude cross-section of the perturbation kinetic energy and the precipitation rate along the latitude 25°N where Kong-rey formed. Both the precipitation and the perturbation energy showed clear westward propagation prior to the genesis of Kong-rey. The wave signals could be traced back 4 to 5 days prior to Kong-rey's formation. The phase speed of the easterly wave was estimated around 4-5 longitude degrees per day.

The vertical cross-section of the easterly wave derived from 3-8-day filtered NCEP-NCAR reanalysis data showed that this easterly wave was quite deep, and had an equivalent barotropic structure [14]. The wave amplitude had two maxima at 600-700hPa and 200-300hPa respectively. This vertical profile was consistent with previous observational studies of easterly wave structures [23].

d. Precursor signals in the middle or upper troposphere

The previous three types of genesis scenarios are primarily related to low level precursor signals. It was found that some TCs did not have significant surface precursor signals; rather they had precursor signals in the middle or upper troposphere.

One such example is Typhoon Usagi, which formed on 9 August 2001. Figure 4 shows that this cyclogenesis event was associated with preexisting cloud activity. Three days prior to the genesis of Usagi, clouds represented by TMI cloud liquid water content had already appeared over the region where Usagi formed.

However, from the 3-8-day filtered QuikSCAT wind fields, there was no clear cyclonic wind perturbation at the surface.

A further analysis of the NCEP final analysis product showed that 2-3 days prior to the TC genesis, a mid-level cyclonic vortex had already set up. The mid-level vortex was accompanied with a weak warm core above and a cold core below, and eventually led to the cyclone development near the surface. This mid-level vortex triggering process has been suggested by Simpson et al. [24], although specific processes that lead to the downward development of cyclonic vorticity are not clear. Numerical simulations in section 4 will further explore this cyclogenesis process.

Some TC genesis events in the WNP may be related to upper tropospheric forcing. Colon examined the evolution of 200hPa flows and found that a poleward flow aloft, such as those in the eastern side of troughs in the westerlies or those in the western side of anticyclones, is a favorable environmental condition for the development of low-level perturbations [25]. Sadler developed a synoptic model to describe the role of the Tropical Upper Tropospheric Trough (TUTT) [26]. He suggested that TUTT might have three effects on TC development. Firstly, the accompanying sub-equatorial ridge on the south side of TUTT lies over the low-level low that may decrease the vertical shear; secondly, a divergent flow on the south and east side of the cyclonic circulation in TUTT may increase the ventilation aloft to help the development of a low-level low; thirdly, a channel to large-scale westerlies may be established for efficient outflow of the heat released by increased convection in the developing depression.

During 2000-2001 summers, three genesis events were associated with the upper tropospheric forcing [14]. An example is Typhoon Nari, which formed on 6 September 2001. Two days prior to its formation, an upper-level trough is located approximately 20 degrees west of the genesis location. One day later, this trough moved eastward 10 longitude degrees. In the mean time, this upper-level trough deepened, and the southwesterly flow on the east side of the trough became stronger. On the genesis date, this trough was within 5 degrees to the northwest of Nari's genesis position. As a result, strong southwesterlies dominated in this area, and an outflow channel was set up in upper levels north of Nari. This led to the enhancement of low-level disturbances and was possibly responsible for Nari's genesis.

3. Origin of WNP synoptic-scale wave trains and easterly waves

Dominant synoptic-scale variability in the WNP is a northwest-southeast oriented synoptic-scale wave train [20]. The wave train extends toward the southeast with a wave-like pattern that consists of alternating regions of cyclonic and anticyclonic

circulations, propagating northwestward. The wave train has a typical wavelength of ~2500 km and a time scale of 6-10 days.

What causes the SWT in the WNP? Li hypothesized that the SWT is an unstable mode of the summer mean flow in the presence of the convection-circulation-moisture (CCM) feedback [27]. To test this hypothesis, an anomaly atmospheric general circulation model (AGCM) was employed. The model was modified from the original version of Princeton global spectrum atmospheric model [28]. It was linearized by a specified 3D basic state (see the appendix of [27] for the detailed derivation of the model and the treatment of circulation-dependent perturbation heating), similar to that of Ting and Yu [29]. Previously this anomaly model was used in studying an asymmetric atmospheric response to equatorially symmetric forcing [30] and MJO initiation in the western Indian Ocean [31].

The model used sigma $(\sigma = p / p_s)$ as its vertical coordinate, and vertically there were 5 evenly distributed sigma levels, with a top level at σ=0 and a bottom level at σ=1. The horizontal resolution was T42. Rayleigh friction was applied to the momentum equations, with the damping rate of 1 day^{-1} taken in the lowest model level $(\sigma = 0.9)$ to mimic the planetary boundary layer (PBL), linearly decaying to 0.1 day^{-1} at the level of $\sigma = 0.7$. Newtonian cooling with an e-folding time scale of 10 days was applied to the temperature equation at all the model levels. Because the focus of the study was on tropical perturbations, a strong damping of 1 day^{-1} was applied in the perturbation momentum and temperature equations over higher latitude regions (beyond 40^{o}N and 40^{o}S). A realistic summer (JJA) mean state of $\bar{u}, \bar{v}, \bar{T}, \bar{P}_s$ was prescribed as the basic state, taken from the long-time mean of the NCEP-NCAR reanalysis.

Initially a small perturbation with a zonal wavenumber-9 structure was introduced. In the presence of both the summer mean flow and the convection-moisture-circulation feedback, the model captured the growth of the most unstable mode in WNP. The fastest growing mode in the model had a typical observed synoptic-scale wave train structure in WNP (see Fig. 5a). The wave train, oriented in the northwest-southeast direction, had alternative cyclonic and anti-cyclonic circulation regions and a zonal wavelength of 2500 km. The preferred geographic location for the perturbation growth appeared in the WNP, primarily due to high moist static energy (MSE) in the region. This is because the background MSE condition would lead to the strongest CCM feedback, given the same perturbation vorticity. The unstable mode, with an eastward tilting vertical structure, propagated northwestward.

In the absence of the CCM feedback, the initial perturbation did not grow; rather it decayed. This indicated that the climatologic summer mean flow alone (without involving of the CCM feedback) was unable to destabilize tropical perturbations.

Thus, the summer mean flow only supported a weakly damped mode in the tropics. This differs fundamentally from mid-latitude baroclinic instability waves, which gain energy directly from the mean westerly jet. The numerical result was consistent with the observational study by Lau and Lau, who pointed out that the primary heat source for the SWT was the latent heating associated with deep convection [32].

Even though the climatologic summer mean flow alone was unable to lead to the perturbation growth, it did play a role in determining the preferred length scale, wave train structure and propagation characteristics. Figure 5b illustrates the meridional wind structure of the least damped mode in the absence of the CCM feedback. A northwest-southeast oriented wave train pattern emerged. The wave train had alternative cyclonic and anti-cyclonic circulation regions, with a wavelength of about 2500 km. The weakly damped mode propagated toward the west and northwest.

Further sensitivity experiments with different initial conditions indicated that the final structure of the unstable mode was not sensitive to the initial conditions. In all cases the model reproduced the most unstable modes that had a synoptic wave train structure similar to that shown in Fig. 5a. This supported the hypothesis that the summertime synoptic wave train in the WNP was a result of instability of the summer mean flow in the presence of the CCM feedback. Any types of perturbations under such a background condition could grow and develop into the wave train pattern.

To reveal the energy accumulation mechanism and dispersion characteristics of Pacific easterly waves, Tam and Li conducted an observational analysis using NCEP-NCAR reanalysis data [33]. A phase-independent wave-activity flux of Takaya and Nakamura [34] was applied to examine the wave activity and energy accumulation associated with PEW. The convergence of the wave activity flux was found in the region of 135-160E, 10-25N. Such convergence could lead to the amplification of Rossby waves, and its pattern was in agreement with the region of positive growth of the observed perturbations.

Negative zonal group velocity associated with the PEW was found everywhere in the WNP, indicative of Rossby wave energy moving to the west at low level. The zonal wavelength of the PEW was estimated. It was found that the zonal wavenumber, k, increased as the wave moves westward. The zonal scale contraction led to the convergence of the group velocity (hence wave activity). There was accumulation of wave activity in the low levels associated with a wave packet of the PEW. The largest contribution to the wave activity accumulation came from the convergence of intrinsic group velocity, which was attributed to the contraction of wavelength toward the west and the change of the horizontal tilt of

waves. By comparison, convergence of the mean flow contributed less to the wave activity accumulation.

It was found that the phase relationship between convection and vorticity depended on longitudinal positions. Signals of enhanced convection were in phase with positive low-level vorticity anomalies west of about 150^{o}E, but to the east the vorticity led the convection by one quarter of a wavelength. This indicated that there were two different dynamical regimes along the 'storm tracks' of synoptic-scale activity. In the eastern portion or at the entrance of the storm tracks, heat flux associated with synoptic-scale eddies was found to be equatorward (i.e. $v'T'<0$) in the mid troposphere. This could be seen in composite maps of circulation as well as eddy covariance statistics.

Associated with the negative heat flux signals was downward injection of wave activity from the upper levels. In the upper troposphere, southward wave activity from the extratropics was able to penetrate into the Tropics near the dateline. Figure 6 is a schematic diagram illustrating 3D energy propagation characteristics associated with PEW. The result suggested that the energy source of Pacific easterly waves originated from mid-latitude Pacific Jet. This hypothesis was supported by a case study in which upper-level activity was able to initiate a synoptic-scale wave train with strong surface circulation features. PV anomalies intruded into the Tropics due to wave breaking were seen to cause downward development, leading to low-level disturbances which subsequently moved westward and grew.

4. Numerical simulations of tropical cyclogenesis

a. TCED induced cyclogenesis

The cyclogenesis associated with TC energy dispersion were simulated in a 3D model. The atmospheric model used in the study was the triply nested movable mesh primitive equation model (TCM3). A detailed description of the model and experiment design can be found in Li et al. [19]. An initial vortex was spun up on a beta-plane for 10 days. The environmental temperature and moisture profiles were the same as those in Wang [35] and represented the mean summertime conditions over the western Pacific. At the end of the 10-day integration, a 3-D Rossby wave train pattern developed. To study the mean flow effect, an idealized monsoon gyre (MG) pattern was specified. This MG had a size of 3000 km and a central minimum pressure 2-3 hPa lower than the surrounding environment. The maximum wind of the MG was about 5 m s^{-1} at a radius of 300 km from the center. Both the pattern and amplitude of the specified MG were quite close to the observed composite [36].

The following three experiments were conducted. In the first experiment (Exp1), the model was initialized with the Rossby wave train only. This experiment was designed to examine whether the wave train alone can develop into a TC in a resting environment. In the second experiment (Exp2), how the background MG evolved with time was examined, without the involvement of the TCED-induced Rossby wave train. In the third experiment (Exp3), the Rossby wave train was superposed on the MG as the initial condition; it was designed to examine whether the wave train-MG interaction could lead to cyclogenesis.

The simulation results (Fig. 7) showed that while the wave train alone or the MG alone did not cause cyclogenesis, the superposition of wave train and MG led to the generation of a new TC. This result suggested that a proper mean flow pattern was essential for the TCED-induced wave train to develop into a TC. The simulated new vortex exhibited realistic TC characteristics, including a tilted eyewall, a warm core, and a vigorous in-up-and-out mean secondary circulation with mean subsidence in the eye region.

Figure 8 shows the evolution of simulated vorticity, relative humidity, vertical velocity and rainfall rate (averaged over a 120 km by 120 km domain centered at the maximum low-level vorticity) in Exp3. Two important features in the vorticity field were worth noting. First, maximum vorticity generation occurred in the PBL, and with the TC development the cyclonic vorticity gradually penetrated from the PBL into the upper troposphere. Secondly, during the initial development stage, the PBL vorticity experienced an oscillatory growth. For instance, the vorticity grew rapidly between hours 60 and 64, slowed down or even decayed afterwards, and re-intensified at hours 72-78. The averaged rain rate also exhibited a clear oscillatory evolution with periods ranged from 9 to 15 hours. This oscillation feature was clearly seen in the vorticity or rainfall field averaged even over a larger domain (e.g., 240 km by 240 km).

The oscillatory vorticity development was closely related to the evolution of vertical motion and relative humidity fields. It can be seen from Fig. 8 that there are alternations of updraft and downdraft, corresponding well to convectively "active" and "break" phases. While the ascending motion associated with penetrated convection led to PBL convergence and thus a positive vorticity tendency, the downdraft led to PBL divergence and thus a negative vorticity tendency. A vorticity budget analysis indicated that the generation of the PBL vorticity in the model was primarily attributed to the divergence term. The vertical motion regulated the moisture profile through vertical moisture transport, leading to the alternative change of relative humidity in mid-troposphere.

The oscillatory development found in the model was validated by observed rainfall and cloud-top temperature evolutions [19]. The diagnosis of the model output showed that the oscillatory development was attributed to the discharge

and recharge of the PBL moisture and its interaction with convection and circulation. The moisture-convection feedback regulated the TC development through controlling the atmospheric stratification, raindrop-induced evaporative cooling and downdraft, PBL divergence, and vorticity generation. On one hand, ascending motion associated with deep convection transported moisture upward and led to the discharge of PBL moisture and a convectively stable stratification. On the other hand, the convection-induced raindrops evaporated, leading to mid-level cooling and downdraft. The downdraft further led to dryness and a reduction of equivalent potential temperature. This reduction along with the recharge of PBL moisture due to surface evaporation led to re-establishment of a convectively unstable stratification and thus new convection.

b. Cyclogenesis efficiency: Mid-level vs. bottom vortex

TC genesis may occur either in an environment with a near bottom vortex (EBV) or an environment with a mid-level vortex (EMV). Which scenario leads to greater genesis efficiency? A cloud-resolving WRF model was used to address this question. The model was quadruply nested. The mesh sizes in all four domains were 181×181 with horizontal grid sizes of 54, 18, 6, and 2 km, respectively. There were 27 levels in the vertical. The Kain-Fritch convective scheme [37] was applied in the two outer meshes and an explicit microphysics scheme [38] was used in the finer meshes. Initial water vapor mixing ratio and other thermodynamic variables were assumed horizontally homogeneous and had the vertical profiles of typical January mean observations at Willis Island, northeast of Australia [39]. The model was set on an *f*-plane centered at 15^{o}N, and a quiescent environment with a constant sea surface temperature (SST) of 29^{o}C was specified. For more detailed model description, readers are referred to [40].

Four experiments were designed. The first experiment (MID_VORTEX) mimicked a mid-level precursor condition, in which initial vortex had a maximum vorticity at 600 hPa, with a maximum wind speed of 8 m s^{-1} at a radius of 100 km and a size of 500 km radius where the wind vanished. The vorticity gradually decreased both upward and downward, and vanished at the surface. In the second experiment (BTM_VORTEX), an initial maximum precursor perturbation with a maximum wind speed of 8 ms^{-1} was located at the surface. Figures 9a and 9b show the vertical-radial cross section of the tangential wind of these initial vortexes. The third and the fourth experiment contained a shallow mid-level vortex (SHAL_MID) and a shallow bottom vortex (SHAL_BTM), respectively, to identify the PBL effects and to better separate the mid-level and the bottom vortices. Their vertical wind profiles are shown in Figs. 9c and 9d.

In all the four experiments, after integration of several days, a TC with realistic dynamic and thermodynamic structures formed. The simulated TC characteristics included a tilted eyewall, a vigorous in-up-and-out secondary circulation, and

subsidence within the eyewall. The maximum tangential wind speed reached to 60 ms^{-1} at a radius of about 20 km. Strong inflow appeared in the PBL, with maximum inflow just outside the radius of the maximum tangential wind. A broad outflow layer appeared in the upper troposphere outside the eyewall.

A marked difference among these experiments was the timing of a rapid pressure drop, suggesting that each event possessed distinct genesis efficiency. Here the genesis time was defined as time when the maximum surface wind reached 17.5 ms^{-1} – a criterion for the tropical storm strength. Figure 10 shows the time evolutions of the corresponding maximum surface wind speed from the four experiments. Based on the definition above, the genesis time occurred at hour 33 for BTM_VORTEX, hour 66 for MID_VORTEX, hour 78 for SHAL_BTM, and hour 114 for SHAL_MID, respectively.

Figure 11 presents the vertical cross section of relative vorticity and temperature anomaly fields averaged over a 100km×100km domain centered at the minimum sea level pressure (MSLP) from the four experiments. In MID_VORTEX, the initial mid-level vorticity maximum coincided well with a cold (warm) core below (above) 600 hPa (top left panel of Fig. 11), due to the thermal wind balance relationship. During the first 30 hours, the mid-level cyclonic vorticity gradually weakened and the "cold core" structure became less distinct. The mid-level vortex re-intensified and created a maximum vorticity center at 500 hPa at hour 48. Associated with this re-establishment of the mid-level vortex was the development of a cold-warm-core couplet and the mid-level convergence. The temperature anomaly (defined as the departure from the mean temperature over the innermost domain) showed a clear cold (warm) anomaly below (aloft) 600 hPa. A weak divergence appeared around 800 hPa before hour 60, implying descending motions and a relative dry layer between 600 and 800 hPa. The thermodynamic structure at hours 48-60 bore the characteristics of stratiform precipitation regime [41], indicating that stratiform cloud was dominated at this time.

The similar plots for BTM_VORTEX were depicted in the bottom left panel of Fig. 11. In this case, a rapid pressure drop occurred after hour 33, indicating faster TC development compared to MID_VORTEX. Although initially the maximum vorticity appeared at the low level, a mid-level vorticity enhancement was observed at hour 30. Associated with this mid-level vorticity enhancement was a cold-warm-core couplet (i.e., a cold core at lower level and a warm core above, bottom left panel of Fig. 11). The temperature and vorticity profiles at that time were associated with a mid-level convergence and downdrafts below, reflecting stratiform cloud regime. Although the TC genesis was slower in the two shallow vortex cases, the vorticity and temperature evolution characteristics in SHAL_MID and SHAL_BTM (right panels of Fig. 11) bore many similarities to their counterparts with deeper vorticity profiles.

A common feature among the EBV and EMV experiments was the formation of a mid-level maximum vorticity prior to TC genesis irrespective where the initial vorticity maximum located. A comparison of the BTM_VORTEX and MID_VORTEX experiments indicated that the former had greater genesis efficiency. A possible cause of this genesis efficiency difference was attributed to the initial column integrated absolute vorticity. Note that the former had greater column-integrated (from 1000 to 200 hPa) absolute vorticity than the latter. Physically, it was argued that vertically integrated absolute vorticity could affect vorticity segregation [42]. To examine additional factors that affected genesis efficiency, two shallow vortex cases (SHAL_BTM and SHAL_MID) were further considered, in which the vertically (1000-200 hPa) integrated absolute vorticity were almost same. The simulation results showed that the cyclogenesis time in SHAL_BTM occurred at hour 78, which was much faster than the genesis time (hour 114) in SHAL_MID. Thus the numerical model results indicated that given the same column integrated absolute vorticity, a bottom vortex was more efficient in cyclogenesis than a mid-level vortex. The difference was likely attributed to the effect of surface fluxes and PBL processes.

A common development characteristic among the four experiments was the occurrence of upscale cascade from randomly distributed cumulus-scale (~5 km) vertical hot towers (VHTs) to an organized meso-vortex-scale (~50-100 km) system (MVS). Sporadic cumulus-scale (~5 km) convective cells developed shortly after the integration started, due to the conditionally unstable environmental condition and the surface evaporation over the ocean. While the cumulus-scale (~5 km) VHTs were randomly triggered initially, they were gradually organized and merged into a MVS through merging around the environmental vorticity center. This warm-core MVS differed from conventional mid-latitude mesoscale convective system that has a distinct cold-core structure. As shown in Fig. 12, in MID_VORTEX, several convective cells moved closer and merged into a larger vortex with the horizontal scale of about 50 km at 48 hour. A similar evolution feature was seen in BTM_VORTEX, although cumulus-scale VHTs and a MVS developed earlier than in MID_VORTEX.

The vorticity segregation proposed by Schecter and Dubin [42] is a possible mechanism for the VHTs merging. That is, cyclonic (anticyclonic) vorticity anomalies move up (down) the ambient vorticity gradient. As a result, cyclonic vorticity anomalies tend to move inward toward the vortex centre, while anticyclonic anomalies tend to move outward away from the centre. This vorticity segregation as well as vortex merger or axisymmetrization [43-45] could cause upscale cascade from cumulus-scale (~5 km) VHTs to a MVS. As seen from all experiments, the upscale cascade was the first key step toward cyclogenesis. Once the MVS system formed, the adjacent convective cells would be further absorbed, or organized into outer spiral rainbands.

Another common development feature was the setup of a deep moist layer prior to cyclogenesis. For instance, in MID_VORTEX, there was a steady increase of the moist layer in the core region during hour 24-60. The 90% RH layer thickened from 900 hPa at hour 24 to about 500 hPa at hour 60. It was the establishment of this near-saturation air column that signified the next development stage: deepening of cyclonic vorticity and a rapid drop of minimum sea level pressure. Such a deepening of the moist layer appeared clearly in the other three experiments.

5. Climatic control of cyclogenesis

In addition to a marked annual cycle, TC genesis frequency in the WNP experiences a significant intraseasonal variation [46-50]. Several studies investigated how the atmospheric intraseasonal oscillation (ISO) modulates TC activity [51-53]. For example, Maloney and Dickinson suggested that the modulation is through enhancing or suppressing the tropical depression (TD)-type disturbances in lower troposphere [53]. The enhancement of the TD-type disturbances is attributed to either Rossby wave accumulation caused by large-scale convergence [54-55] or barotropic energy conversion during ISO westerly phases [52-53].

The large-scale control of the ISO on the WNP cyclogenesis in 2000 and 2001 summers was examined by Fu et al. [14]. The pattern and the characteristics of the ISO were represented by the 20-70-day filtered OLR and 850hPa zonal wind fields. Both the wind and OLR fields were widely used to represent ISO activity in many previous studies. Observational analyses showed that the ISO was characterized by enhanced (suppressed) convection and westerly (easterly) in 850hPa zonal wind in its active (suppressed) phase. From a thermodynamic perspective, enhanced convection provided a greater large-scale low-level moisture convergence that favored the development of tropical depressions. From a dynamic perspective, the ISO westerly anomaly helped increase the cyclonic vorticity to the north and created favorable environment for tropical depression development. As a result, more TCs formed in the active phase of ISO.

The time series of area-averaged (5^{o}N-25^{o}N, 110^{o}E-160^{o}E) OLR perturbations are shown in the left panels of Fig. 13. There were two ISO events in the WNP each year. The active phase (negative OLR perturbations) occurred from 28 June to 15 July and from 6 August to 5 September in 2000, and from 16 June to 6 July and 8 August to 26 August for year 2001. Figure 13 also shows area averaged OLR and zonal wind perturbations on the 34 cyclogenesis date in 2000 and 2001. It appears that most of TC geneses events in 2000 and 2001 were coincided with ISO active phases.

The relationship between the barotropic energy conversion and the TC genesis location during active and suppressed ISO phases are shown in Fig. 14. Positive conversion appeared in both the ISO active and suppressed phases, indicating that synoptic-scale disturbances always obtained kinetic energy from the total background mean (including ISO) flow [56]. Regions of enhanced barotropic conversion favored the development of synoptic seed disturbances, which could further grow into TCs. It was noted that TCs tended to form in the positive barotropic energy conversion regions. The amplitude and spatial pattern of the energy conversion varied with the ISO phase. During the ISO active phase, larger energy conversion occurred over the WNP south of 25°N (Fig. 14a). During the ISO suppressed phase, positive conversion with smaller amplitude appeared over the WNP (Fig. 14b). The TC genesis number in the WNP was approximately proportional to the barotropic energy conversion. For example, the TC genesis number during the ISO active phase was 43, 1.5 times greater than that during the ISO suppressed phase (27). A similar ratio appeared in the barotropic energy conversion amplitude.

What determined the interannual variation of TC genesis number in the WNP? A calculation of the simultaneous correlation between JJAS TC number and Nino3.4 index during 1979-2010 showed a positive value, but the simultaneous correlations were not statistically significant, from both Hadley and NOAA SST datasets (Table 1). Lagged correlations of JJAS TC number with the Nino3.4 index in the preceding winter (DJF 0) and in the succeeding winter (DJF +1), however, were both statistically significant at the 95% level. The correlation with the Nino3.4 in the preceding winter was negative. This indicates that TC frequency decreased (increases) during El Nino (La Nina) decaying summer. The correlation with the Nino3.4 in the succeeding winter was positive, indicating that TC frequency increased (decreased) during El Nino (La Nina) developing summer.

The observed TC number at each of El Nino developing and decaying summers is shown in Fig. 15. The average TC number during 1979-2010 was 15.75. Six out of eight El Nino developing summers had more than normal TC frequency, with exceptional cases in 2006 and 2009. Six out of seven El Nino decaying summers (except in 1988) were characterized by less than normal TC frequency in the WNP. The ENSO-phase-dependent feature was quite consistent with Iizuka and Matsuura, who analyzed the ENSO-TC relationship in a coupled atmosphere-ocean general circulation model [57].

What caused the ENSO-phase-dependent cyclogenesis feature? During the El Nino developing summer, equatorial westerly anomalies appeared in the central Pacific, which strengthened cyclonic shear and led to the southeastward shift of the monsoon trough. As seen from total and anomalous 850-hPa vorticity fields

(Fig. 16), a maximum low-level vorticity belt extended southeastward. In the anomaly field, a large-scale negative vorticity anomaly occupied the WNP typhoon genesis region. The southeastward shift of the monsoon trough led to more frequent TC genesis in the southeast quadrant of the WNP [58]. During the El Nino decaying summer, a large-scale anomalous anticyclone appeared in the WNP (bottom panel of Fig. 16). This led to a weakening of the WNP monsoon trough. The ENSO-phase-dependent background flow condition caused distinctive behaviors in atmospheric ISO, with a stronger (weaker) ISO variability during the El Nino developing (decaying) summer [59]. Thus the change of the large-scale background condition (including both the mean flow and ISO variability) was responsible for the opposite TC changes during ENSO developing and decaying summers.

Previous studies proposed a set of universal TC genesis parameters [60-61]. Given distinctive mean flow and disturbance characteristics in NATL and WNP, it is likely that factors controlling cyclogenesis differ. Peng et al. and Fu et al. investigated the differences of developing versus non-developing tropical disturbances using global daily analysis fields of the Navy Operational Atmospheric Prediction System (NOGAPS) from year 2003 to 2008 [62-63]. A box difference index (BDI) was introduced to quantitatively measure the differences between the developing and non-developing disturbances. The definition of the index is as below:

$$BDI = \frac{M_{DEV} - M_{NONDEV}}{\sigma_{DEV} + \sigma_{NONDEV}}$$

where M_{DEV} and σ_{DEV} (M_{NONDEV} and σ_{NONDEV}) represent the mean and standard deviation of a variable for the developing (non-developing) cases.

To illustrate what a BDI value means, they took relative humidity as an example and considered a simple case that the standard deviations of the developing and non-developing groups were same. Figure 17 shows what it looks like in a box-and-whiskers figure when BDI is 0, 0.5 and 1. It is obvious that BDI=0 implies that there is no difference between the two groups. BDI=1 denotes a case in which the developing and non-developing groups are well separated, whereas BDI=0.5 implies that the two groups are partially separated.

With the aid of the BDI, Peng et al. and Fu et al. objectively evaluated how important a genesis parameter was in distinguishing developing and non-developing disturbances [62-63]. Larger BDI amplitude implies a greater possibility to differentiate the developing and non-developing groups. Using this objective method, they ranked key genesis parameters at the NATL and WNP basins.

Table 2 lists top ranked genesis parameters in the NATL and the WNP based on their BDI calculations. It is interesting to note that the top three parameters in the NATL belong to the thermodynamic factor. For example, the vertically integrated specific humidity from 925hPa to 400hPa ranks the top of all the parameters, while the rain rate and SST follow as the second and the third most important parameters in NATL. In contrast, major genesis parameters in the WNP (except the rain rate) belong to the dynamic factors. Therefore, the BDI may provide a basis for selecting predictors for a statistical TC genesis forecast model at each basin.

6. Projected future TC changes in North Pacific

How global warming will affect TC activity is a hotly debated topic [64-66]. With the increase of the global SST and surface moisture, it was anticipated that more TCs would develop. However, many climate models simulated a global decreasing trend of TC frequency [67-72]. One explanation of the decreasing trend was attributed to an increase of atmospheric static stability. This is because the global warming leads to a larger increase of air temperature in the upper troposphere than in the lower troposphere; as a result, the atmosphere becomes more stable, which suppresses the TC frequency [67, 72]. Does the same mechanism affect the regional TC change?

Li et al. investigated the cause of regional TC changes in the Pacific under global warming based on two high-resolution global AGCMs [73]. The first AGCM used was ECHAM5 [74] at a horizontal resolution of T319 (about 40-km grid). SST, the lower boundary condition of the model, was derived from a lower-resolution (T63) coupled version of the model (ECHAM5/MPI-OM) [75], which participated in the fourth assessment report of intergovernmental panel for climate change (IPCC-AR4). Two different climate change scenarios (20C3M and A1B) were applied. In 20C3M scenario, increasing historical greenhouse gases in 20th century were prescribed as a radiative forcing. In A1B scenario, carbon dioxide concentration was increased at a rate 1% per year till it reached 720 ppm and was then kept constant. A ‘time-slice’ method [76] was applied, in which the high-resolution AGCM was forced by SST during two 20-year periods (1980-1999 and 2080-2099). The two periods are hereafter referred to as 20C and 21C, respectively. The second model was the GFDL high-resolution (50-km) atmospheric model (HiRAM2.1). For detailed model description and its simulation of the annual, inter-annual and decadal variations of TC activity, readers are referred to [77]. HiRAM2.1 was forced by an ensemble SST warming pattern in 21C derived from 18 IPCC AR4 models. It is worth mentioning that the two AGCMs have distinctive physical parameterization schemes in convection and radiation.

Figure 18 shows the difference of TC genesis frequency between the 20C and 21C simulations. In 20C, TCs form primarily over the western and eastern Pacific, similar to the distribution of the observed genesis locations. In 21C, however, more TCs shift their genesis locations to the Central Pacific. As seen from the difference map, there are two notable TC decrease and increase regions over the Pacific. One is over the WNP and the other the central North Pacific (CNP). In the ECHAM5 simulation, the numbers of TCs in 21C decreases by 31% over WNP but increases by 65% over CNP. Similarly, HiRAM2.1 projects a 30% decrease of TC genesis number in WNP but a 19% increase in CNP. Thus both the high-resolution AGCMs with distinctive model physics and different SST warming patterns simulate two opposite TC trends in WNP and CNP. Further HiRAM2.1 simulations with different future SST warming patterns derived from GFDL CM2.0 and CM2.1, HADCM3, HADGEM1, ECHAM5, CCCMA, MRIGCM, and MIROCHI confirmed that the west-east shift of TC genesis location in the North Pacific is indeed a robust signal (Ming Zhao, personal communication).

To understand the cause of this west-east shift, Li et al. diagnosed the dynamic and thermodynamic conditions in northern summer (July – October) over the WNP (5-25ºN, 110ºE-160ºE) and CNP (5-25ºN, 180-130ºW) regions, respectively. The change of atmospheric stability parameter was examined. The result showed that the upper-level air temperature increased at a greater rate than that at lower levels in both the regions. As the static stability is measured by the vertical gradient of the potential temperature, the result implies that the atmosphere becomes more stable under the global warming in both the regions. Thus, the static stability change cannot explain the opposite trends of TC frequency between WNP and CNP.

A further analysis revealed that the fundamental cause of the opposite TC trends lies in the change of dynamic conditions. As we know, TCs originate from the tropical disturbances such as synoptic wave trains and easterly waves. The 21C simulation showed an increased variability of synoptic-scale disturbances over the NCP region but a decreased synoptic activity over the NWP region. Here the strength of the synoptic-scale disturbances was represented by the variance of the 850-hPa vorticity field filtered at a 2-8 day band using Lanzcos digital filter [78]. Both the models showed a remarkable decrease of the synoptic-scale variance over WNP but an increase of the variance in CNP. Thus, it is likely that the decreasing trend in NWP is caused by the reduced synoptic-scale activity whereas the increasing trend in NCP is caused by the strengthening of synoptic disturbances.

The contrast of the synoptic-scale activity between WNP and CNP possibly resulted from the change of the background vertical wind shear and low-level

divergence (Fig. 19). Previous theoretical and modeling works pointed out that the easterly shear and low-level convergence of the background mean flow favored the development of tropical disturbances [79-80, 27]. In the 20C simulation, the western Pacific and Indian monsoon regions have a prevailing easterly wind shear in association with large-scale convective heating. This easterly wind shear becomes weaker in the warming climate (Fig. 19a). The weakening of the easterly wind shear corresponds to a weakened western Pacific monsoon, as seen from Fig. 19b. The weakening of the easterly shear, along with low-level divergence to its east (Fig. 19c), further suppresses the development of tropical disturbances in WNP. In contrast, the easterly wind shear and low-level convergence in CNP are strengthened, and so is the precipitation. They favor the development of TCs in CNP.

It was argued that the change of the background vertical shear and the low-level divergence was closely related to changes of the trade wind in the tropics (Fig. 19c). Many IPCC-AR4 models predicted an El Nino-like warming pattern in the Pacific under global warming [81], that is, a greater SST warming would occur in the tropical eastern and central Pacific compared to that in the tropical western Pacific. As a result, the zonal SST gradient was reduced across the tropical Pacific. The reduced zonal SST gradient would decrease the trade wind [82] and weaken the Walker circulation. The weakening of the trades would lead to the decrease of the boundary-layer convergence in the western Pacific monsoon region and the increase of the boundary convergence in CNP (Fig. 19c). The former would suppress the monsoon convective heating and decrease the easterly shear in WNP, whereas the latter would strengthen the local boundary layer moisture convergence and convective heating and thus increase the easterly wind shear in CNP.

7. Conclusion

This chapter summarizes some of recent progress in understanding tropical cyclogenesis in the WNP from both synoptic and climatic aspects. Observational analyses indicate that synoptic precursor perturbations at low levels in the WNP include TC energy dispersion induced Rossby wave trains, northwest-southeast oriented synoptic wave trains, and Pacific easterly waves. This feature differs from that in the NATL where dominant precursor signal is African easterly wave. In addition the near surface precursor signals, some cyclogenesis events are associated with a mid-level vortex or TUTT.

Dominant synoptic-scale variability in the WNP is a southeast-northwest oriented synoptic wave train. A theoretical study suggested that this wave train was originated from the instability of the summer mean flow in the presence of the

convection-circulation feedback in the WNP. The structure and dispersion characteristics of the Pacific easterly wave were examined through the diagnosis of observational data. A wave activity diagnosis showed that the zonal scale contraction primarily contributes to the convergence of the wave activity, while the convergence of the mean flow contributes less to the wave activity accumulation. An analysis of group velocity in the upper troposphere and in the vertical direction showed that there was downward injection of wave activity from the upper levels and in the upper troposphere wave activity directed southward form the extratropics to the tropical central Pacific. The result indicated that the energy source of Pacific easterly waves originated from mid-latitude Pacific Jet.

The cyclogenesis associated with TCED was simulated in a 3D model. A new TC with realistic dynamic and thermodynamic structures formed in the wake of a pre-existing TC when a large-scale monsoon gyre was present. Maximum vorticity generation appeared in the PBL and the vorticity growth exhibited an oscillatory development. This oscillatory growth was also seen in the observed rainfall and cloud-top temperature fields. The diagnosis of the model output showed that the oscillatory development was attributed to the discharge and recharge of the PBL moisture and its interaction with convection and circulation. A cloud-resolving (2-km grid) model was used to investigate cyclogenesis efficiency in an environmental mid-level and bottom vortex. The simulation results showed that a bottom vortex was more efficient in cyclogenesis than a mid-level vortex, given the same column integrated absolute vorticity. Both the mid-level and bottom vortex experiments shared common development characteristics: 1) a transition from random cumulus-scale (~5 km) convective cells into an organized meso-vortex-scale (~50 km) system through upscale cascade, 2) a setup of a nearly saturated air column prior to a rapid drop of the central minimum pressure, and 3) a convective-stratiform phase transition.

TC frequency in the WNP is regulated by ISO activity. The number of TCs increases (decreases) during an active (suppressed) phase of ISO. Cyclogenesis activity is also El Nino-phase dependent. The TC genesis number increases (decreases) during El Nino developing (decaying) summer. A Box Difference Index was used to rank major genesis parameters that were capable of differentiating the developing and non-developing disturbances. It was found that whereas TC genesis in the NATL was more sensitive to the thermodynamic factors, dynamic factors played a major role in determining whether or not a tropical disturbance would develop in the WNP.

The future change of TC genesis location in the North Pacific under global warming was investigated with use of two global high-resolution models

(ECHAM5 T319 and GFDL HiRAM2.1). A significant shift was found in the location of TCs from the western to central North Pacific. The shift to more cyclones in the central Pacific and less in the western Pacific was not attributable to a change in atmospheric static stability, but to a change in the variance of tropical synoptic-scale perturbations associated with a change in the background vertical wind shear and boundary layer divergence.

Acknowledgments. The author appreciates two anonymous reviewers for constructive comments. Contributions by Drs. Melinda Peng, Pangchi Hsu, Bing Fu, Xuyang Ge, Francis Tam, MinHo Kwon, and Ming Zhao are greatly appreciated. This work was supported by ONR grants N000140810256 and N000141010774, NSF grant AGS-1106536, NOAA grant NA11OAR4310087, and by the International Pacific Research Center that is sponsored by the Japan Agency for Marine-Earth Science and Technology (JAMSTEC), NASA (NNX07AG53G) and NOAA (NA17RJ1230). This is SOEST contribution number 8484 and IPRC contribution number 816.

References

[1] R. A. Anthes, Tropical cyclone: their evolution, structure and effects. *Meteor. Mongr.* No. **41**, *Amer. Meteor. Soc.*, 208pp, (1982).

[2] G. R. Flierl, *J. Phys. Oceanogr*.,**14**, 47, (1984).

[3] G. R. Flierl and K. Haines, *Phys. Fluids*, **6**, 3487, (1994).

[4] Z. Luo, *Acta Meteor. Sinica*, **8**, 51, (1994).

[5] N. R. McDonald, *J.Fluid Mech.*, **361**, 237, (1998).

[6] L.E. Carr III and R.L. Elsberry, NPS Tech. Rep. NPS-MR-94-002, 273 pp, (1994).

[7] L.E. Carr III and R.L. Elsberry, *Mon. Wea. Rev*. **123**, 265, (1995).

[8] X. Ge, T. Li., Y. Wang, and M. Peng, *J. Atmos. Sci.*, **65**, 2272, (2008).

[9] W. M. Frank, *Mon.Wea.Rev*., **110**, 572, (1982).

[10] N. E. Davidson and H. H. Hendon, *Mon.Wea.Rev*. **117**, 1458, (1989).

[11] L. M. Briegel and W.M. Frank, *Mon. Wea. Rev*. **125**, 1397, (1997).

[12] E. A. Ritchie and G. J. Holland, *Mon.Wea.Rev*., **125**, 1377, (1997).

[13] T. Li, B. Fu, X. Ge, B. Wang, and M. Peng, *Geophy. Res. Let*., **30**, 2122, (2003).

[14] B. Fu, T. Li, M.S. Peng, and F.Z. Weng, *Wea. Forecasting*, **22**, 763, (2007).

[15] G. R. Flierl, M. E. Stern and J. A. Whitehead, Jr., *Dyn. Atmos. Oceans*, **7**, 233, (1983).

[16] T. Li and B. Fu, *J. Atmos. Sci.* **63**, 1377, (2006)

[17] L. J. Shapiro and K. V. Ooyama, *J. Atmos. Sci.*, **47**, 170, (1990).

[18] X. Ge, T. Li, and X. Zhou, *Geophys. Res. Lett.*, **34**, L23807, doi:10.1029/2007GL031867, (2007).

[19] T. Li, X. Ge, B. Wang, and Y. Zhu, *J. Atmos. Sci.*, **63**, 1390, (2006).

[20] K.-H. Lau and N.-C. Lau, *Mon. Wea. Rev.*, **118**, 1888, (1990).

[21] Y. N. Takayabu and T. Nitta, *J. Meteor. Soc. Japan*, **71**, 221, (1993).

[22] M. Dickinson and J. Molinari, *J. Atmos. Sci*. **59**, 2183, (2002).

[23] R. J. Reed and E. E. Recker, *J. Atmos. Sci.*, **28**, 1117, (1971). R. J. Reed, D. C. Norquist, and E. E. Recker, *Mon. Wea. Rev.*, **105,** 317, (1977).

[24] J. Simpson, E. Ritchie, G. J. Holland, J. Halverson, and S. Stewart, *Mon. Wea. Rev*., **125**, 2643, (1997).

[25] J. A. Colon and W.R. Nightingale, *Mon. Wea. Rev*. **91**, 329, (1963).

[26] J. C. Sadler, *Mon. Wea. Rev.*, **104**, 1266, (1976).

[27] T. Li, *J. Atmos. Sci.* **63**, 1093, (2006).

[28] I. M. Held, and M. J. Suarez, *Bull. Amer. Meteor. Soc*., **75**, 1825, (1994).

[29] M. Ting and L. Yu, *J. Atmos.Sci*., **55**, 3565, (1998).

[30] B. Wang, R. Wu, T. Li, *J. Climate*, **16**, 1195, (2003).

[31] X. Jiang and T. Li, *J. Climate*, **18**, 3777, (2005).
[32] K.-H. Lau and N-C. Lau, *Mon. Wea. Rev.*, **120**, 2523, (1992).
[33] C.-Y. Tam and T. Li, *Mon. Wea. Rev*., **134**, 1630, (2006).
[34] K. Takaya and H. Nakamura, *J. Atmos. Sci.*, **58,** 608, (2001).
[35] Y. Wang, *Mon. Wea. Rev.*, **129**, 1370, (2001).
[36] E. A. Ritchie and G. J. Holland, *Mon. Wea. Rev.*, 127, 2027, (1999).
[37] J. S. Kain and J. M. Fritsch, *J. Atmos. Sci.*, **47**, 2784, (1990).
[38] Y.-L. Lin, R. D. Rarley, and H. D. Orville, *J. Appl. Meteor.*, **22**, 1065, (1983).
[39] G. J. Holland, *J. Atmos. Sci.*, **54,** 2519, (1997).
[40] X. Ge, T. Li and M. Peng, *J. Tropical Meteorology*, in press (2012).
[41] S. E. Yuter and R. A. Houze, Jr., *Mon. Wea. Rev.*, **123**, 1941, (1995).
[42] D. A. Schecter and D. H. Dubin, *Phys. Rev. Lett.*, **83**, 2191, (1999).
[43] E. A. Hendricks, M. T. Montgomery, and C. A. Davis, *J. Atmos. Sci.*, **61**, 1209, (2004).
[44] M. T. Montgomery, M. E. Nicholls, T. A. Cram, and A. B. Saunders, *J. Atmos. Sci.*, **63**, 355, (2006).
[45] K. J. Tory, M. T. Montgomery, and N. E. Davidson, *J. Atmos. Sci.*, **63**, 3077, (2006).
[46] W. M. Gray, *Meteorology over the Tropical Oceans*, D. B. Shaw, ED., Royal Meteorological Society, 155, (1979).
[47] N. Yamazaki and M. Murakami, *J. Meteor. Soc. Japan*, **67**, 791, (1989).
[48] D. L. Hartmann, M. L. Michelsen, and S. A. Klein, *J. Atmos. Sci.*, **49**, 1277, (1992).
[49] H. Liebmann, H. Hendon, and J. D. Glick, *J. Meteor. Soc. Japan*, **72**, 401, (1994).
[50] E. D. Maloney and D. L. Hartmann, *J. Climate*, **13**, 1451, (2000).
[51] E. D. Maloney and D. L. Hartmann, *J. Atmos. Sci.*, **58**, 2545, (2001).
[52] A. H. Sobel and E. D. Maloney, *Geophys. Res. Lett.*, **27**, 1739, (2000).
[53] E. D. Maloney and M. J. Dickinson, *J. Atmos. Sci.*, **60**, 2153, (2003).
[54] G. J. Holland, *Meteor. Atmos. Phys.*, **56**, 57, (1995).
[55] A. H. Sobel and C. S. Bretherton, *J. Atmos. Sci.*, **56**, 3106, (1999).
[56] P.-C. Hsu, T. Li, and C.-H. Tsou, *J. Climate*, **24**, 927, (2011).
[57] S. Iizuka, and T. Matsuura, *Clim.Dyn*., 30, 815, (2008).
[58] B. Wang and J. C. L. Chan, *J. Climate*, **15**, 1643, (2002).
[59] A. Lin and T. Li, *J. Climate*, **21**, 6304, (2008).
[60] W. M. Gray, *Mon. Wea. Rev.*, **96**, 669, (1968).
[61] K. A. Emanuel and D. S. Nolan, *26th Conference on Hurricanes and Tropical Meteorology*, Am. Meteorol. Soc., Miami, FL, (2004).
[62] M. Peng, B. Fu, T. Li, and D. E. Stevens, *Mon.Wea.Rev*., in press (2012).

[63] B. Fu, M. Peng, T. Li, and D. E. Stevens, *Mon.Wea.Rev*., in press (2012).
[64] P. J. Webster, G. J. Holland, J. A. Curry, and H.-R. Chang, *Science*, **309**, 1844, (2005).
[65] K. A. Emanuel, *Nature*, **436**, 686, (2005).
[66] C. W. Landsea, B. A. Harper, K. Hoarau, and J. A. Knaff, *Science*, **313**, 452, (2006).
[67] M. Sugi, A. Noda, and N. Sato, *J. Meteorol. Soc. Japan*, **80**, 249, (2002).
[68] R. E. McDonald, and coauthors, *Clim. Dyn.*, **25**, 19, (2005).
[69] A. Hasegawa, and S. Emori, *Scientific Online Letters on the Atmosphere*, **1**, 145, (2005).
[70] J. Yoshimura, M. Sugi, and A. Noda, *J. Meteorol. Soc. Japan*, **84**, 405, (2006).
[71] K. Oouchi, and coauthors, *J. Meteorol. Soc. Japan*, **84**, 259, (2006).
[72] L. Bengtsson, K. I. Hodges, M. Esch, N. Keenlyside, L. Komblush, J. J. Luo, and T. Yamagata, *Tellus* **59A**, 539, (2007).
[73] T. Li, M. Kwon, M. Zhao, J.-S. Kug, J.-J. Luo, and W. Yu, *Geophys. Res. Lett.*, **37**, L21804, doi:10.1029/2010GL045124, (2010).
[74] E. Roeckner, and coauthors, Max Planck Institute for Meteorology Rep. 349, 127 pp, (2003).
[75] H. Jungclaus, and coauthors, *J. Climate*, **19**, 3952, (2006).
[76] L. Bengtsson, M. Botzet, and M. Esch, *Tellus*, **48A**, 57, (1996).
[77] M. Zhao, I. M. Held, S.-J. Lin, and G. A. Vecchi, *J. Climate*, **22**, 6653, (2009).
[78] C. E. Duchon, *J. Appl. Meteoro.* **18**, 1016, (1979).
[79] B. Wang and X. Xie, *J. Atmos. Sci.*, **53**, 449, (1996).
[80] K. P. Sooraj, D. Kim, J.-S. Kug, S.-W. Yeh, F-F. Jin, and I.-S. Kang, *Clim. Dyn.*, **33**, doi 10.1007/s00382-008-0483-6, (2008).
[81] S. Solomon, and coauthors, *Cambridge University Press for the Intergovernmental Panel on Climate Change*, (2007).
[82] R. S. Lindzen and S. Nigam, *J. Atmos. Sci.*, **44**, 2440, (1987).

Table 1 Correlation coefficients between JJAS TC number in the WNP and Nino3.4 index at preceding winter (DJF 0), concurrent summer (JJAS), and succeeding winter (DJF+1) during 1979-2010. The first raw shows the correlation coefficients using raw SST data from the Hadley Center and NOAA. The second raw indicates the correlation coefficients using the linearly-detrended SST fields from the same data sources. Bold numbers indicate correlation coefficients significant at the 0.05 level.

		DJF 0	JJAS	DJF+1
Raw SST	Hadley	**-0.36**	0.25	**0.37**
	NOAA	**-0.37**	0.28	**0.35**
Detrended SST	Hadley	**-0.36**	0.26	**0.37**
	NOAA	**-0.35**	0.29	**0.36**

Table 2 List of top four genesis parameters in the NATL and the WNP based on the BDI rank. "**T**" and "**D**" in the bracket denote the thermodynamic factor and the dynamic factor respectively.

Basin / BDI rank	NATL	WNP
1	925 - 400hPa water vapor content (**T**)	800hPa maximum relative vorticity (**D**)
2	Rain rate (**T**)	Rain rate (**T**)
3	SST (**T**)	1000-400hPa averaged $\partial u / \partial y$ (**D**)
4	700hPa maximum relative vorticity (**D**)	1000-500hPa averaged divergence (**D**)

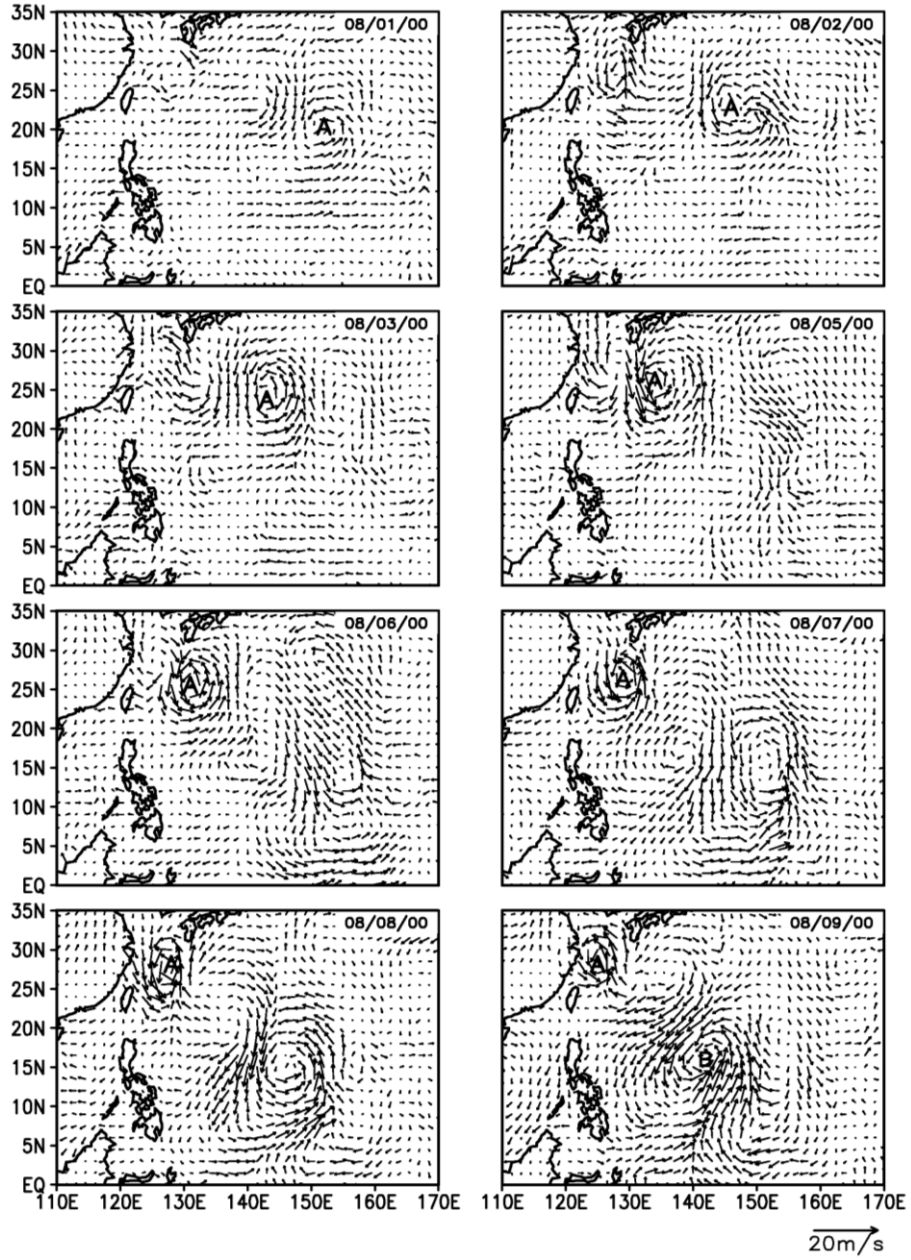

Fig. 1 Time sequences of synoptic-scale surface wind patterns associated with the Rossby wave energy dispersion of Typhoon Jelawat. “A” represents the center location of Jelawat that formed on 1 August 2000. “B” represents the center location of a new TC named Ewiniar that formed on 9 August 2000 in the wake of the Rossby wave train of Jelawat. (From [14], (c)American Meteorological Society, reprinted with permission.)

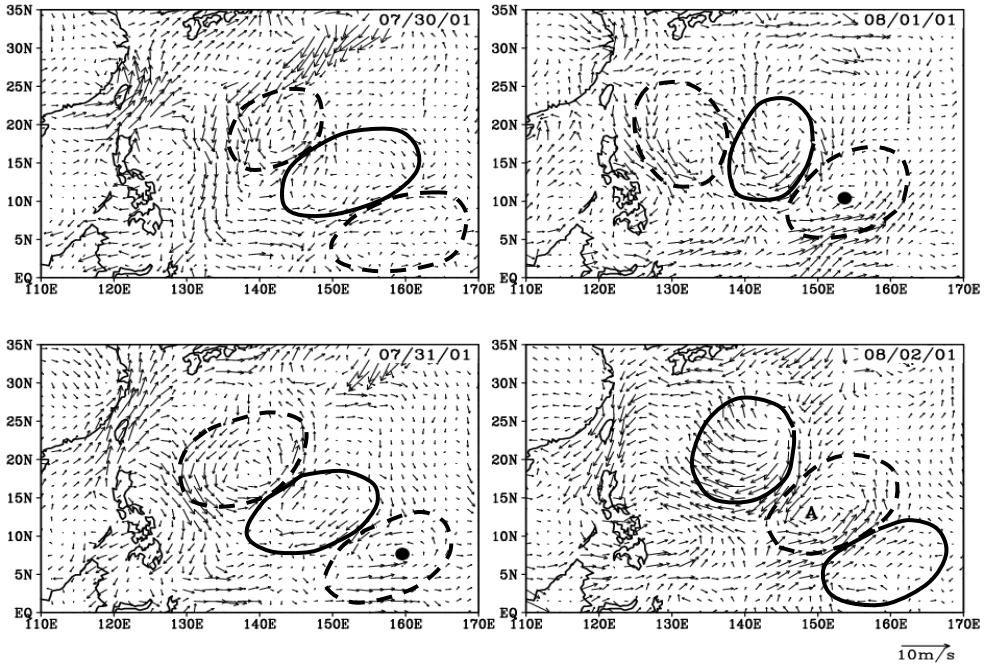

Fig. 2 Time evolution of 3-8-day filtered QuikSCAT surface wind patterns associated with synoptic wave train. The dots indicate the center location of cyclonic circulation prior to genesis of typhoon "Man-yi"; "A" indicates the center location of typhoon "Man-yi" on the day of genesis. Cyclonic/anticyclonic circulation is marked with dashed/solid circle. (From [14], (c)American Meteorological Society, reprinted with permission.)

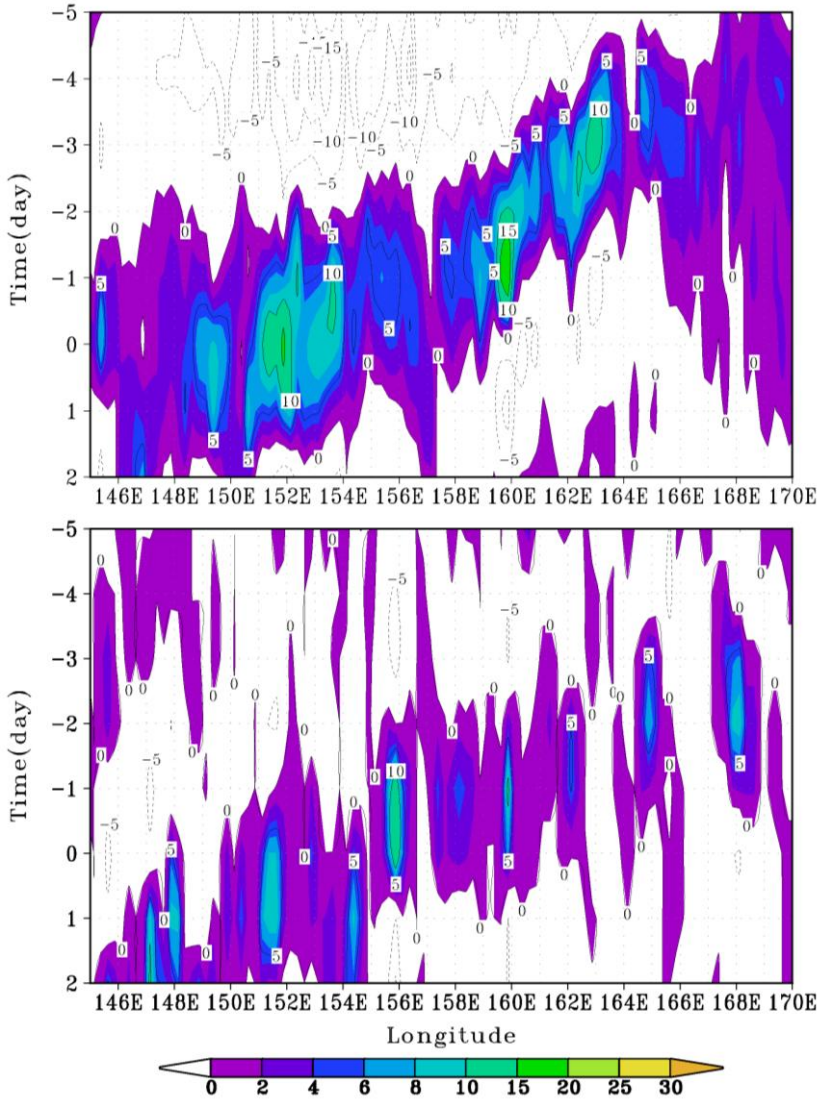

Fig. 3 Time-longitude profiles of the surface kinetic energy $(u^2 + v^2)'/2$ (upper panel, units: m^2s^{-2}) and precipitation rate (lower panel, units: mm day^{-1}) along 25°N. The horizontal axis is longitude and the vertical axis is time in days. Typhoon Kong-rey formed at 150.2°E, 25°N on 22 Jul 2001 (corresponding to day 0). Both panels show clear westward-propagating signals prior to the birth of Kong-rey. (From [14], (c)American Meteorological Society, reprinted with permission.)

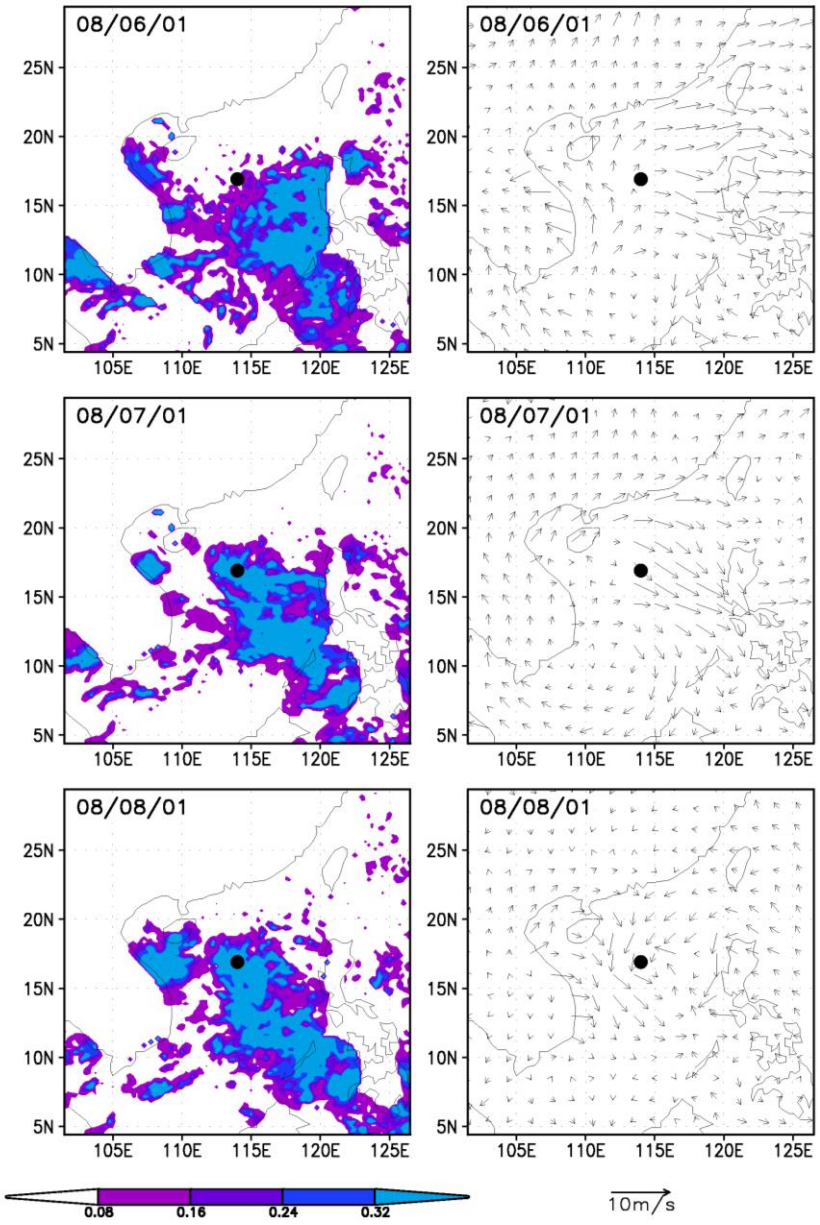

Fig. 4 Time evolution of TMI cloud liquid water (left) and 3-8-day filtered QuikSCAT surface wind (right) prior to the genesis of TC Usagi. Usagi formed on 9 Aug 2001. The dots indicate the position where Usagi formed. (From [14])

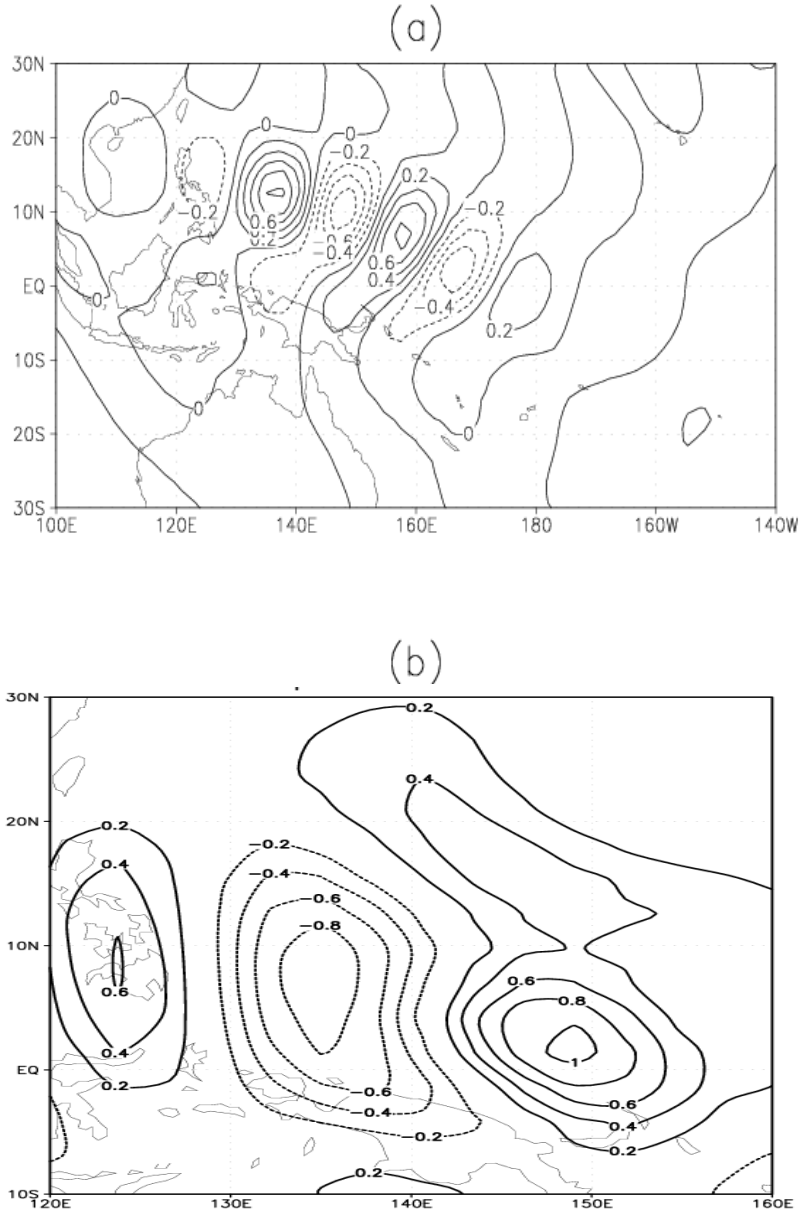

Fig. 5 Horizontal patterns of normalized meridional wind fields at σ=0.7 (contour interval: 0.2) associated with (a) the most unstable mode in the presence of the CMC feedback and (b) the least damped mode in the lack of the CMC feedback. (From [27], (c)American Meteorological Society, reprinted with permission.)

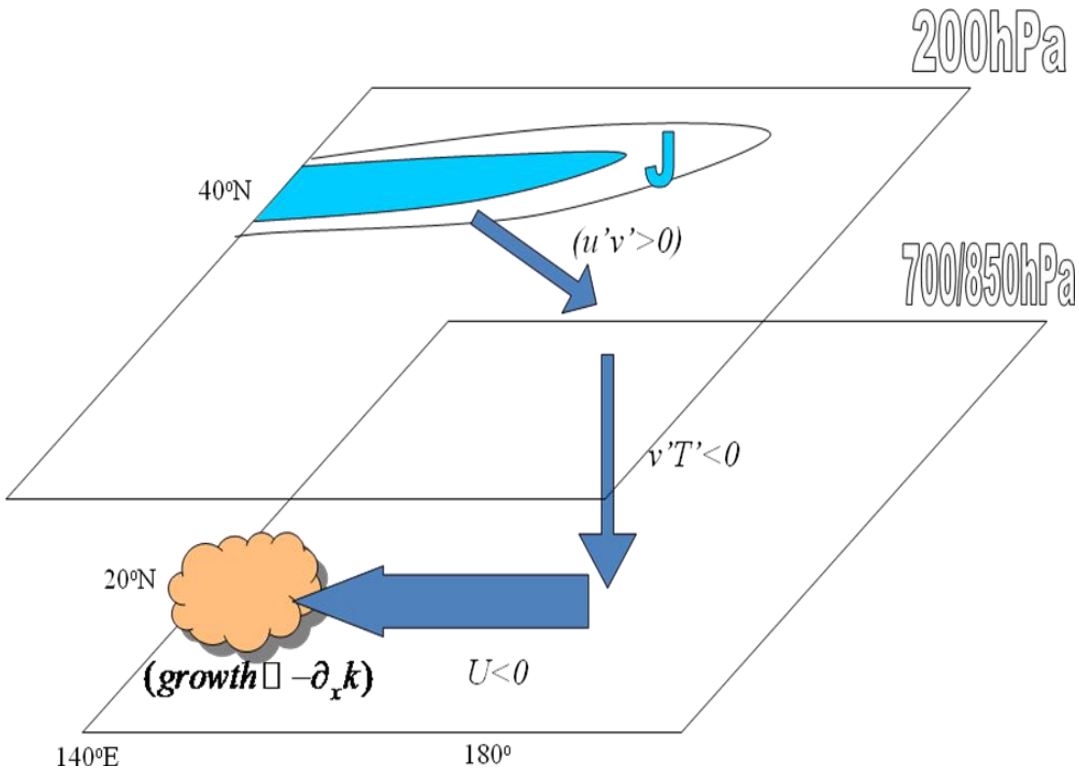

Fig. 6 A schematic diagram illustrating the southward wave energy propagation from the mid-latitude Pacific Jet to tropical central Pacific, downward energy propagation in the tropical central Pacific, and westward wave activity flux in the lower troposphere over the western North Pacific. Both wave scale contraction and confluent mean flows contribute to the energy accumulation of easterly waves in the maximum perturbation growth region (135E-160E, 10-25N).

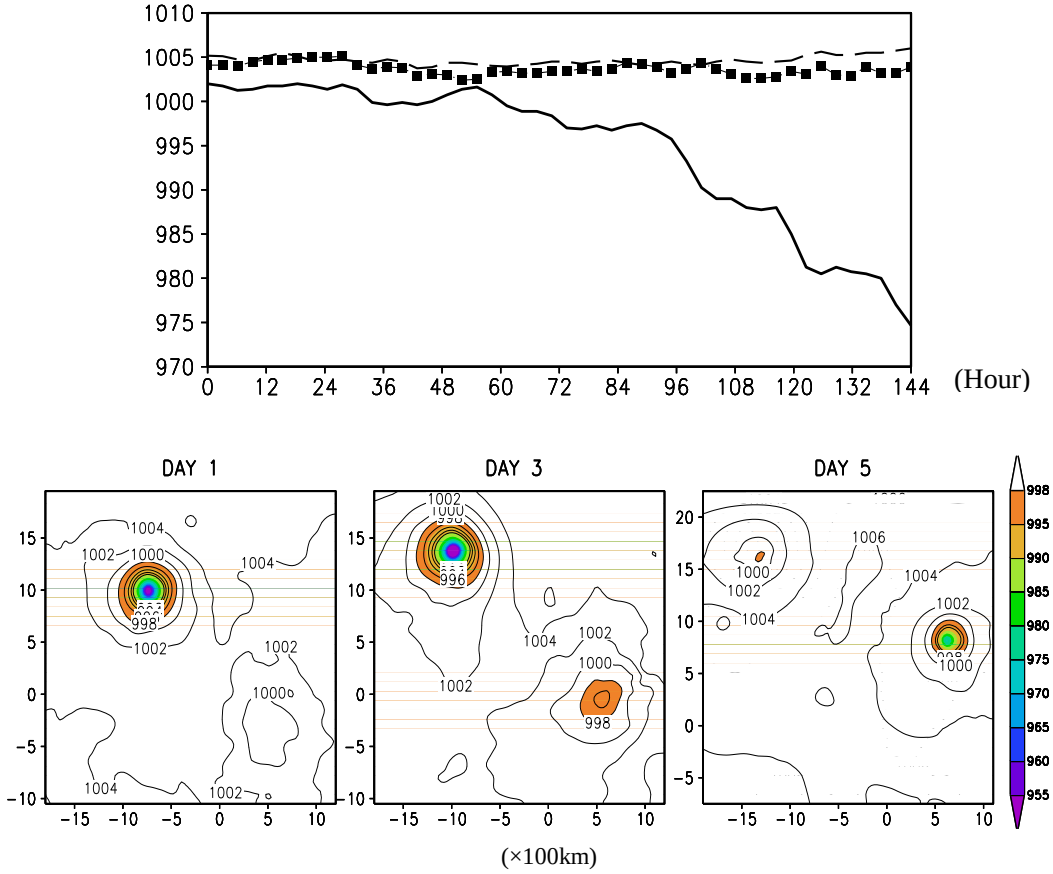

Fig. 7 Time evolution of minimum sea-level pressure fields (upper panel) for Exp1 (dashed line), Exp2 (dotted line) and Exp3 (solid line). The lower panels show the surface pressure (unit: hPa) patterns at day 1, 3 and 5 in Exp3. (From [19], (c)American Meteorological Society, reprinted with permission.)

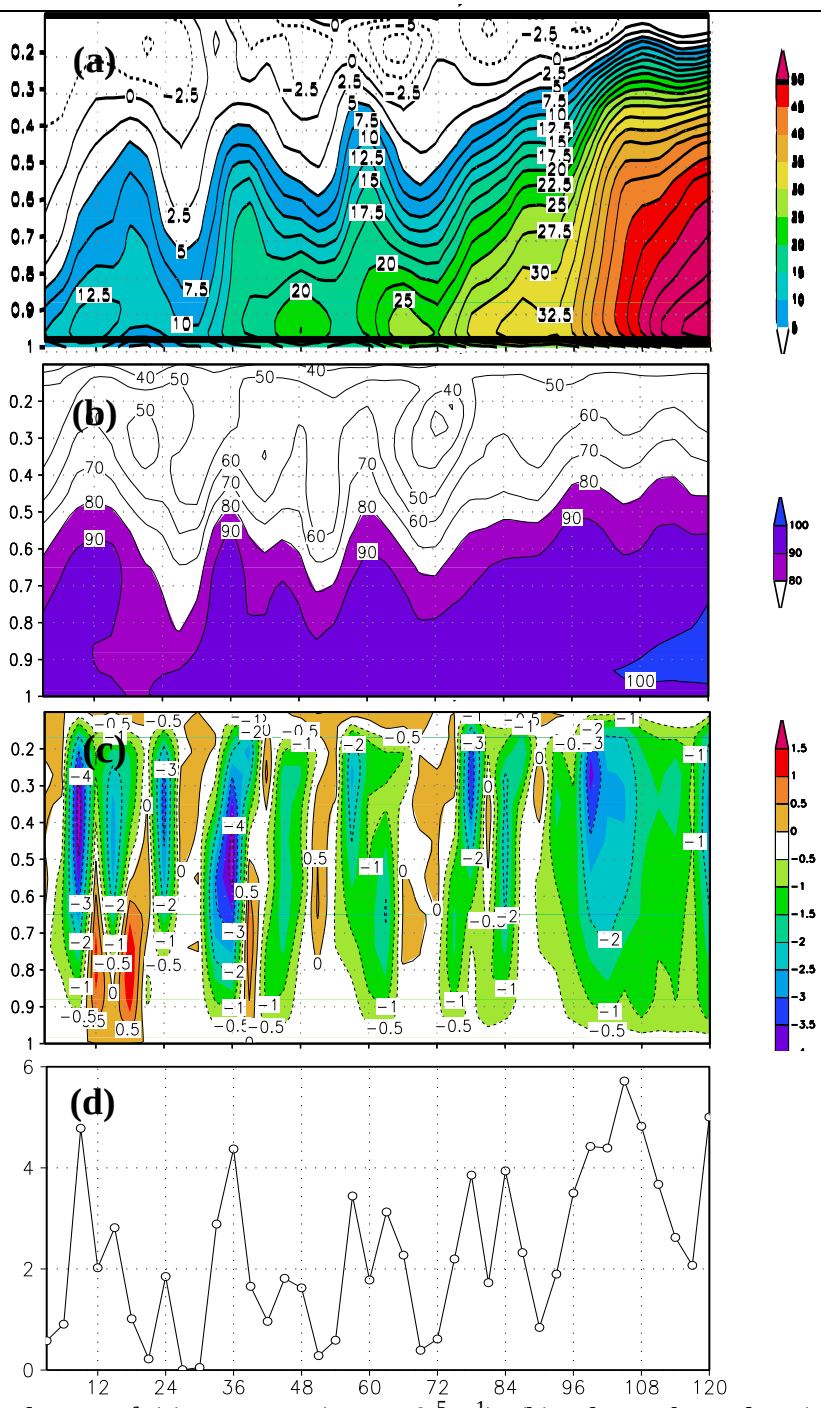

Fig. 8 Time evolution of (a) vorticity (unit: 10^{-5} s^{-1}), (b) relative humidity (unit: %), (c) vertical motion (unit: 10^{-5} s^{-1}) and (d) rainfall rate (unit: mm/hr) averaged over a 120 km by 120 km domain centered at the low-level maximum vorticity in Exp3. The horizontal axis is time (unit: hours) and the vertical axis in (a)-(c) is the sigma level. (From [19], (c)American Meteorological Society, reprinted with permission.)

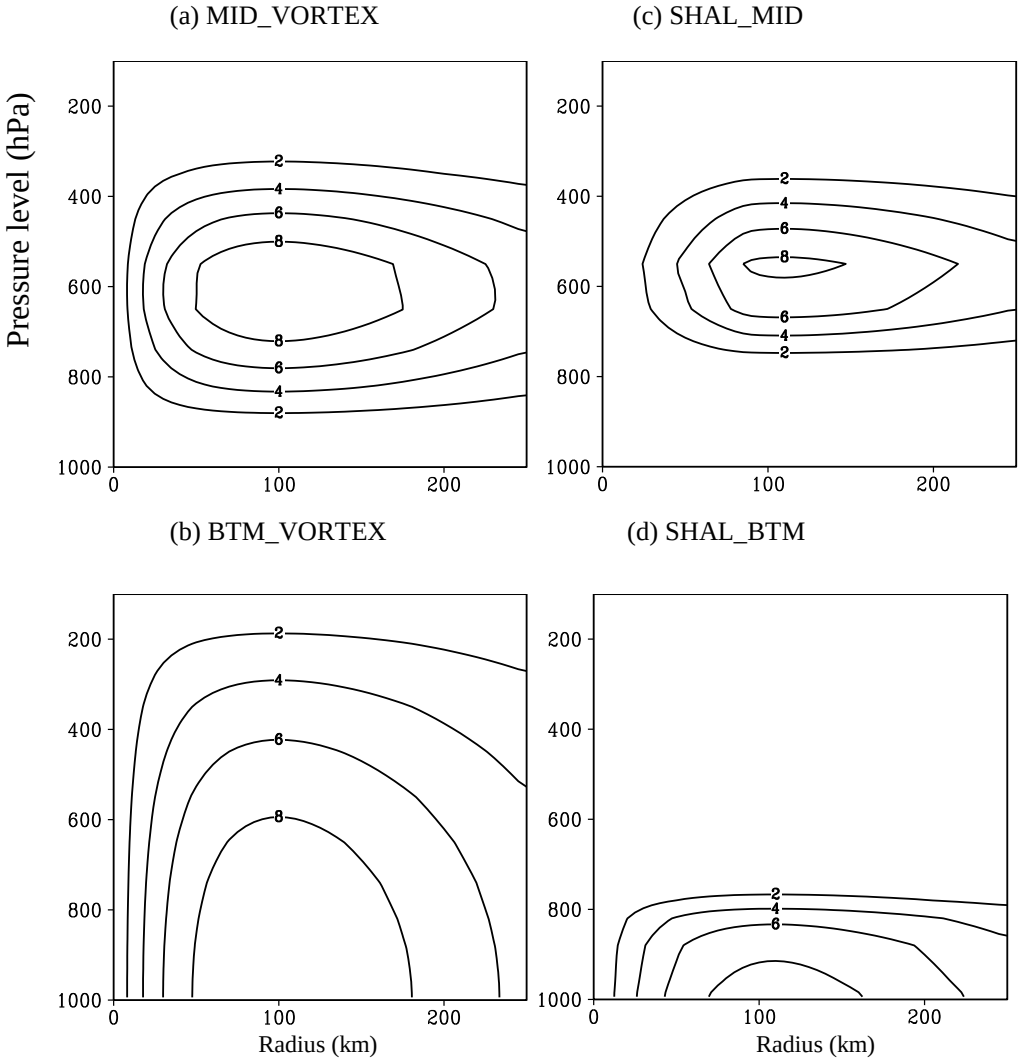

Fig. 9 The vertical-radial cross section of tangential velocity (ms^{-1}) of the initial vortex in (a) MID_VORTEX, (b) BTM_VORTEX, (c) SHAL_MID and (d) SHAL_BTM. (From [40])

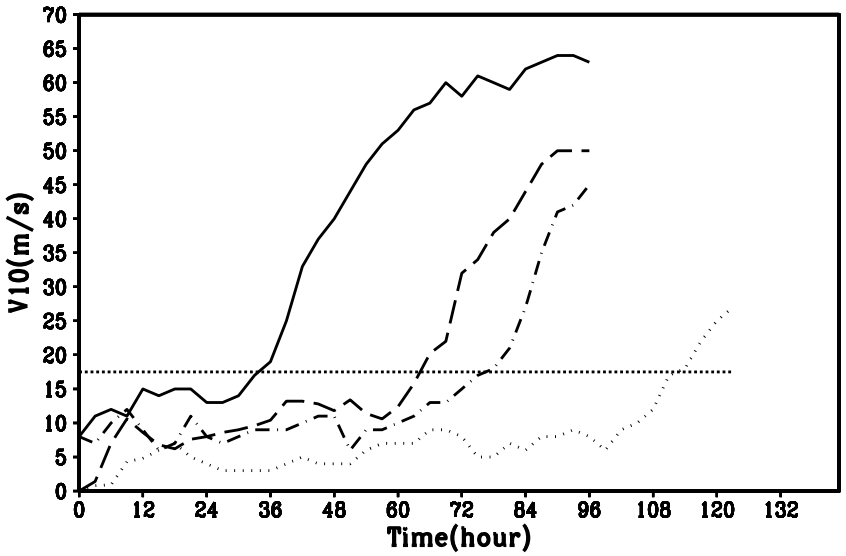

Fig. 10 Time evolution of the simulated maximum surface wind speed in BTM_VORTEX (solid line), MID_VORTEX (dashed line), SHAL_BTM (dot-dashed line) and SHAL_MID (dotted line). The horizontal dotted line in the bottom panel indicated the threshold of TC genesis when the wind speed reaches 17.5 ms^{-1}. (From [40])

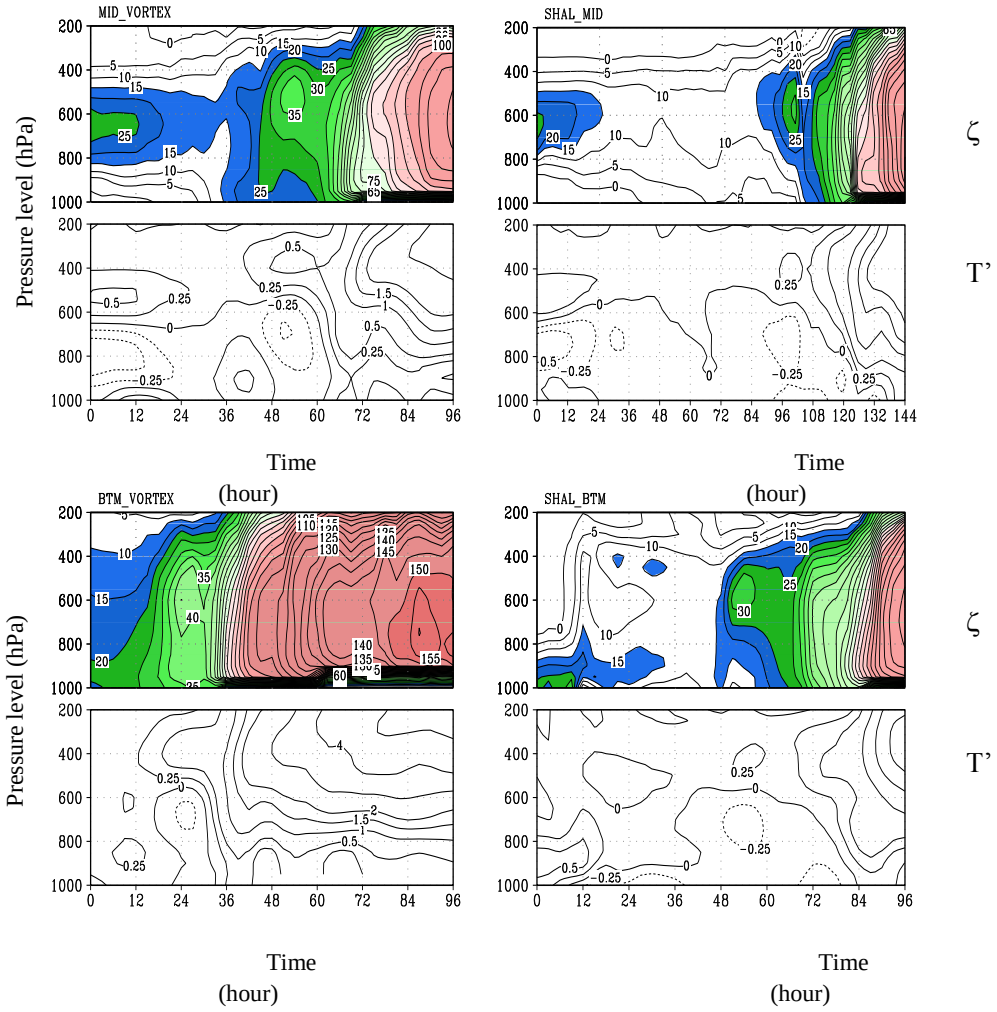

Fig. 11 Time-vertical (unit: hPa) cross section of relative vorticity (1×10^{-5} s^{-1}) and temperature anomaly (K) averaged over a 100 km×100km domain centered at the MSLP in MID_VORTEX (top left), BTM_VORTEX (bottom left), SHAL_MID (top right) and SHAL_BTM (bottom right). (From [40])

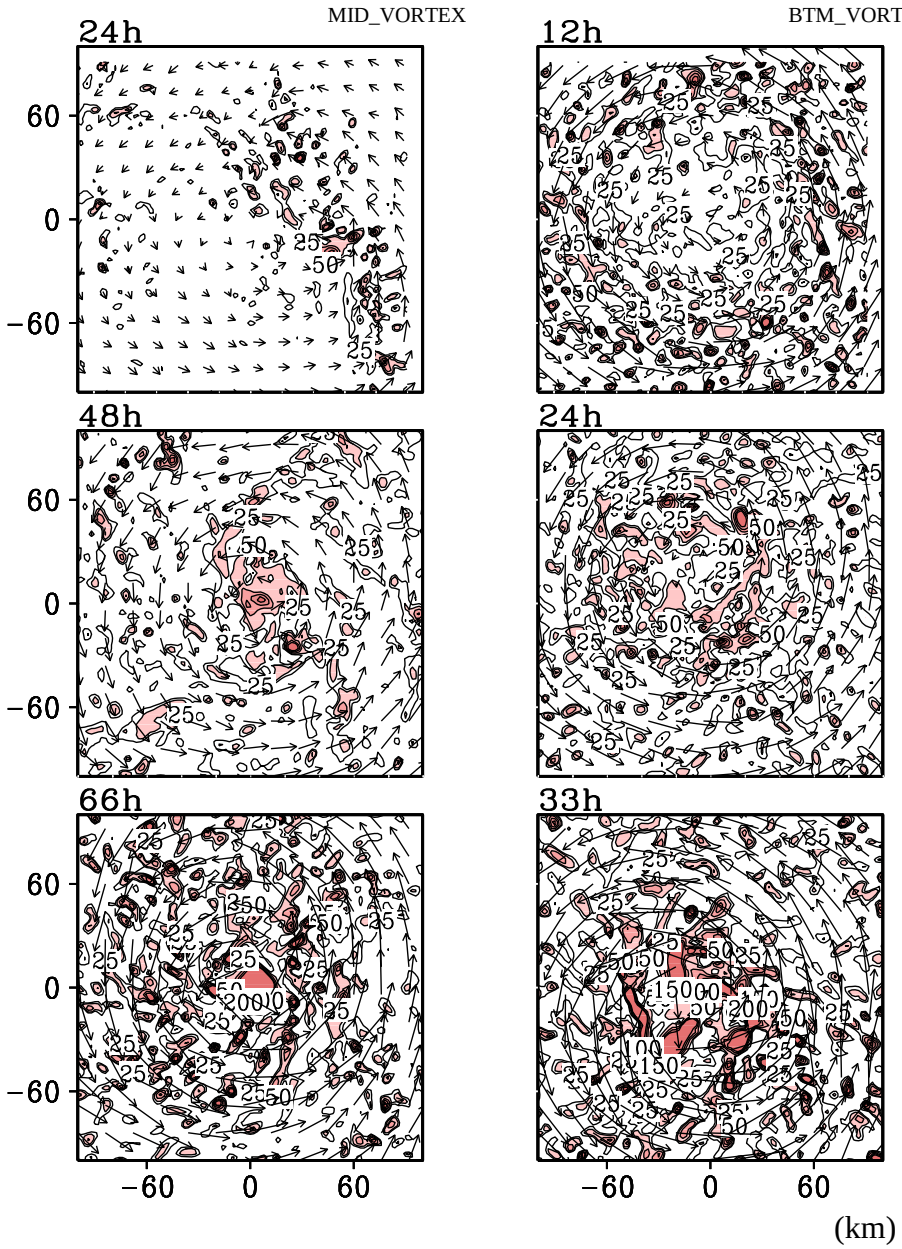

Fig. 12 Horizontal patterns of low-level (900hPa) wind field (vector) and relative vorticity (greater than $3\times10^{-4}s^{-1}$ are shaded) in MID_VORTEX (left) and BTM_VORTEX (right). (From [40])

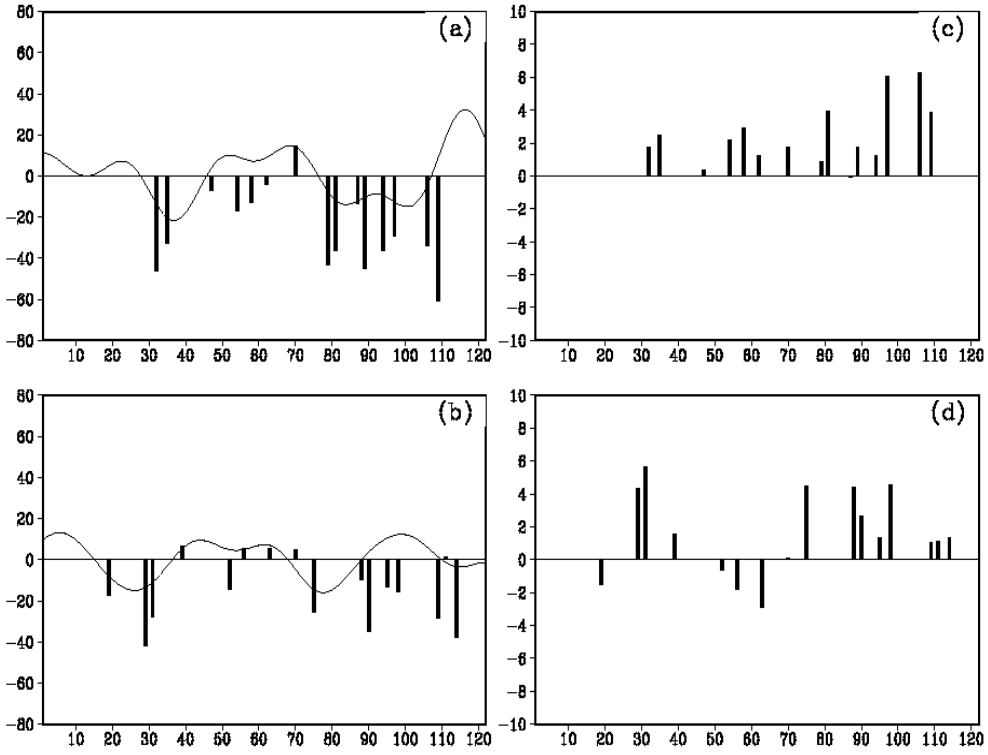

Fig. 13 The 20-70-day filtered OLR (unit: W/m^2) (left panels) and 850mb zonal wind (unit: m/s) (right panels) in 2000 (upper panels) and 2001 (lower panels) as a function of time (From 1 Jun to 30 Sep, totally 122 days). Each bars represents the OLR or zonal wind perturbations at the location of TC genesis when TCs occur. The curves in the left panels are time series of 20-70-day filtered OLR averaged in the domain (5^{o}N-25^{o}N, 110^{o}E-160^{o}E). (From [14], (c)American Meteorological Society, reprinted with permission.)

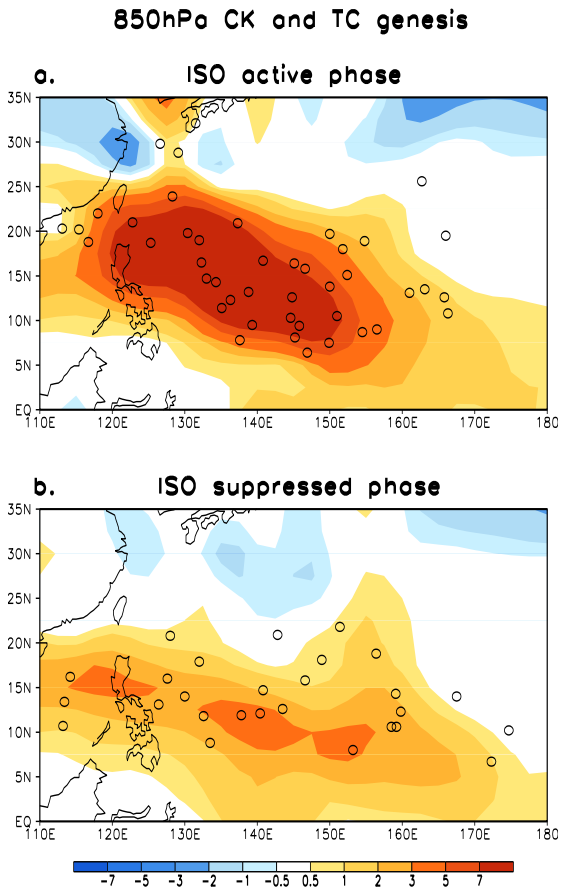

Fig. 14 Composites of 850-hPa barotropic energy conversion field (shading, unit: 10^{-5} m^2s^{-3}) and TC genesis location (circle) during the ISO (a) active and (b) suppressed phase (From [56], (c)American Meteorological Society, reprinted with permission.)

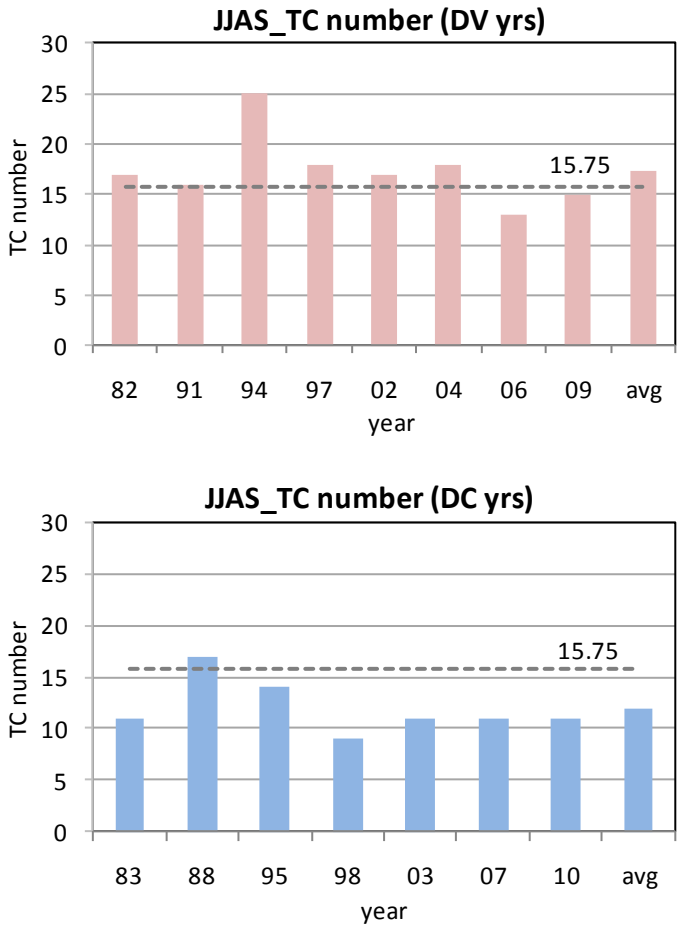

Fig. 15 JJAS tropical cyclone number in the WNP during the El Niño developing years (upper panel) and dacaying years (bottom panel). The dashed line with number indicate the climatological TC number for 1979-2010.

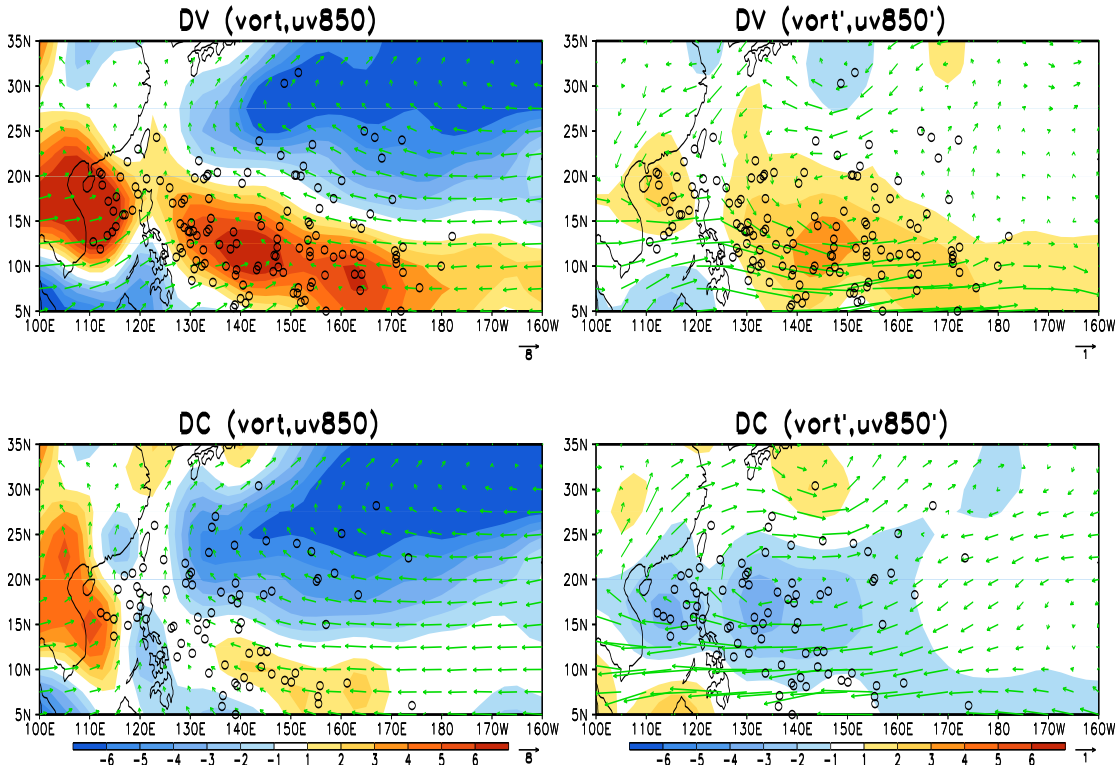

Fig. 16 Left: Composites of 850-hPa vorticity (shading, unit: 10^{-6} s^{-1}), wind field (vector, unit: m s^{-1}) and TC genesis location (circle) for the El Niño developing years (upper) and dacaying years (bottom). Right: Same as left panel except that the shadings and vectors represent the anomalous vorrticity and wind fields, respectively.

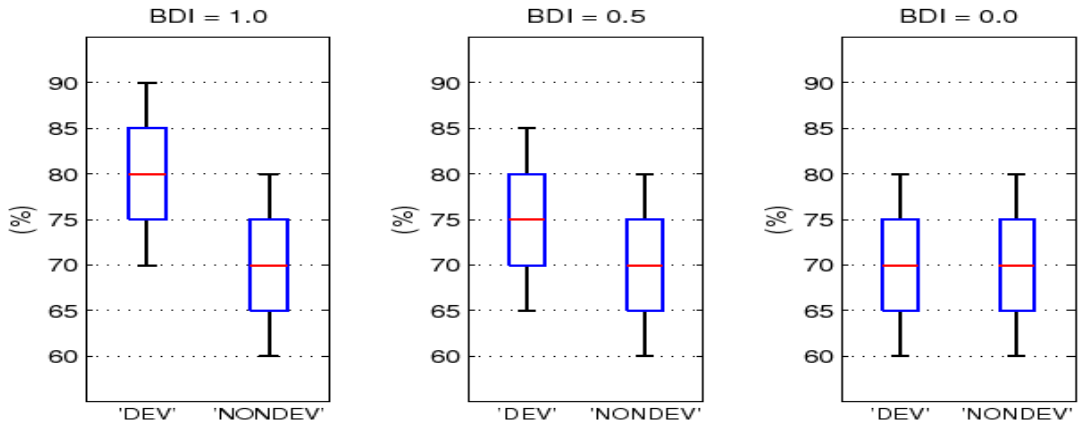

Fig. 17 Idealized box-and-whiskers figures for BDI=1.0, 0.5 and 0. The red line denotes the mean value of a genesis parameter (say, relative humidity at 500 hPa), the blue box represents the standard deviation of the parameter within the developing (denoting as 'DEV') and non-developing (denoting as 'NONDEV') disturbance groups. Whiskers (black line) represent the minimum and maximum of the samples. (From [62], (c)American Meteorological Society, reprinted with permission.)

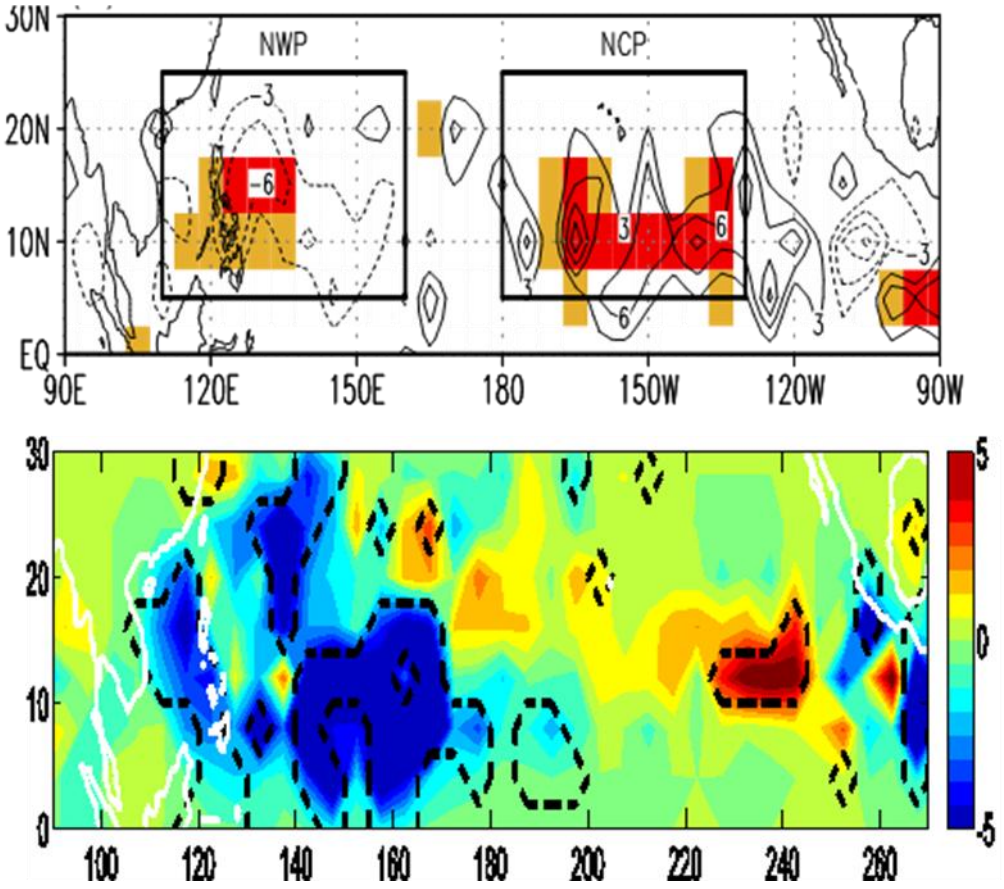

Fig. 18 Differences (21C minus 20C) of TC genesis number at each 2.5°x2.5° box for a 20-year period derived from the ECHAM5 T319 (top) and HiRAM2.1 (bottom). In the top panel, red (orange) shaded areas indicate 95% (90%) confidence level. In the bottom panel, dashed line denotes the 95% confidence level. (From [73], Copyright [2010] American Geophysical Union, reproduced by permission of American Geophysical Union.)

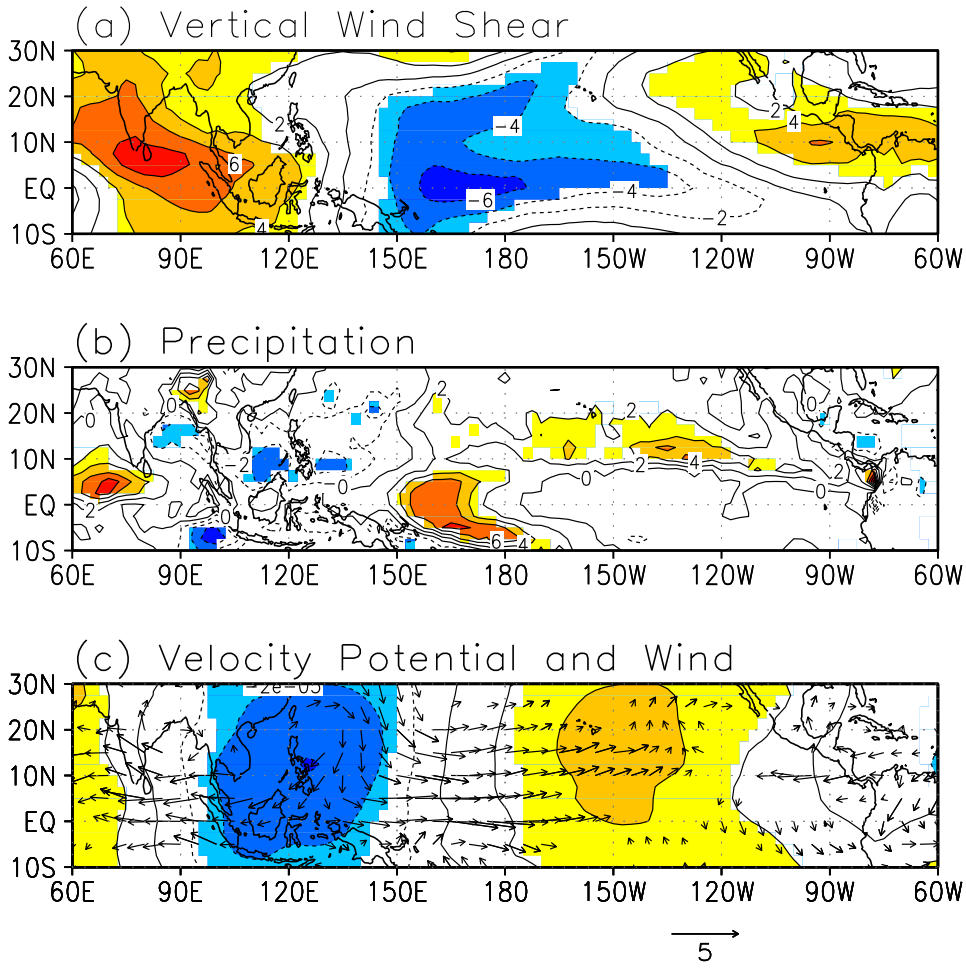

Fig. 19 Difference (21C – 20C) fields of (a) the vertical shear of zonal wind (200 hPa minus 850 hPa, unit: m s^{-1}), (b) precipitation (unit: mm day^{-1}), and (c) velocity potential (unit: s^{-1}) and wind (unit: m s^{-1}) at 850 hPa during northern summer (July-October). Areas that exceed the 95% confidence level (Student's *t* test) are shaded (for contour) and plotted (for vector). (From [73], Copyright [2010] American Geophysical Union, reproduced by permission of American Geophysical Union.)